Cell Metabolism

Article

Glucose-dependent insulinotropic polypeptide receptor signaling in oligodendrocytes increases the weight-loss action of GLP-1R agonism

Graphical abstract

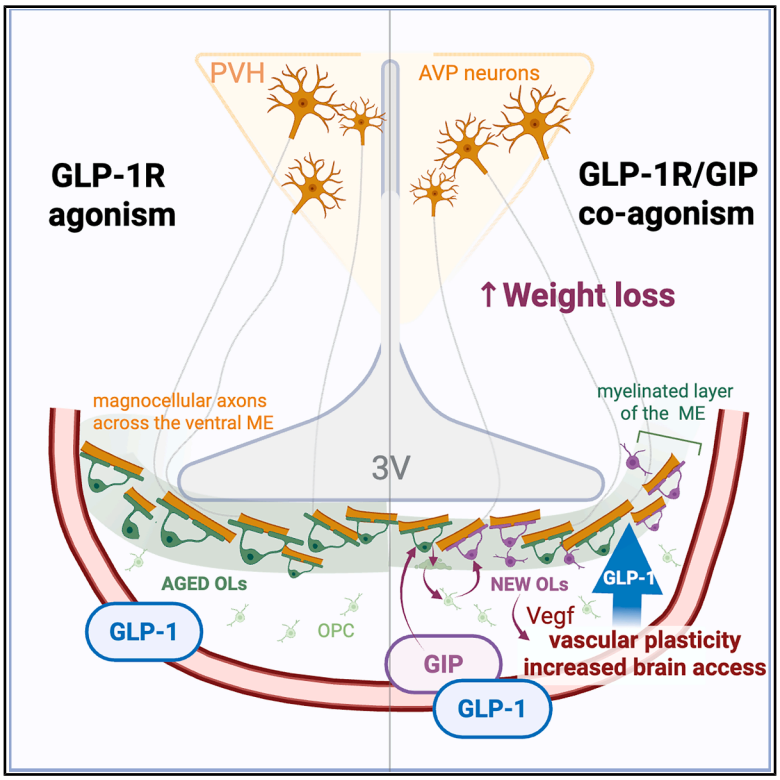

Highlights

- GIPR in oligodendrocytes (OLs) regulates median eminence (ME) oligodendrogenesis
- GIPR in OLs is required for full weight-loss efficacy of GIPR/GLP-1R co-agonism
- GIP increases brain access of GLP-1R agonists to vasopressin axons in the ME
- PVH vasopressin neurons are required for GLP-1R-agonist-induced weight loss

Authors

Robert Hansford, Sophie Buller, Anthony H. Tsang, ..., Alice Adriaenssens, Soyoung Park, Clemence Blouet

Correspondence

csb69@medschl.cam.ac.uk

In brief

Hansford et al. show that GIPR, a target of new weight-loss drugs, is found in brain cells called oligodendrocytes. GIPR helps these drugs access the brain and boosts weight loss. Without GIPR in these cells, the drugs are less effective, revealing a new mechanism behind their action.

Hansford et al., 2025, Cell Metabolism *37*, 1820–1834
September 2, 2025
https://doi.org/10.1016/j.cmet.2025.07.009

CellPress

CellPress
OPEN ACCESS

Cell Metabolism

Article

Glucose-dependent insulinotropic polypeptide receptor signaling in oligodendrocytes increases the weight-loss action of GLP-1R agonism

Robert Hansford,[1,7] Sophie Buller,[1] Anthony H. Tsang,[1] Simon Benoit,[1] Anna G. Roberts,[4] Emmy Erskine,[1] Thomas Brown,[1] Valentina Pirro,[2] Frank Reimann,[1] Norio Harada,[3] Nobuya Inagaki,[3] Ricardo J. Samms,[2] Johannes Broichhagen,[5] David J. Hodson,[6] Alice Adriaenssens,[4] Soyoung Park,[2] and Clemence Blouet[1,8,*]

[1]Wellcome-MRC Institute of Metabolic Science, Addenbrooke's Hospital, Cambridge CB20QQ, UK
[2]Diabetes, Obesity and Complications, Lilly Research Laboratories, Eli Lilly and Company, Indianapolis, IN, USA
[3]Department of Diabetes, Endocrinology and Nutrition, Kyoto University, Kyoto, Japan
[4]Department of Neuroscience, Physiology, and Pharmacology, University College London, London, UK
[5]Leibniz-Forschungsinstitut für Molekulare Pharmakologie (FMP), 13125 Berlin, Germany
[6]Oxford Centre for Diabetes, Endocrinology and Metabolism (OCDEM), NIHR Oxford Biomedical Research Centre, Churchill Hospital, Radcliffe Department of Medicine, University of Oxford, Oxford, UK
[7]Present address: Metsera, Inc. New York, NY
[8]Lead contact
*Correspondence: csb69@medschl.cam.ac.uk
https://doi.org/10.1016/j.cmet.2025.07.009

SUMMARY

The next generation of obesity medicines harness the activity of the glucose-dependent insulinotropic polypeptide and glucagon-like peptide 1 receptors (GIPR and GLP-1R), but their mechanism of action remains unclear. Here, we report that the GIPR is enriched in oligodendrocytes and GIPR signaling bidirectionally regulates oligodendrogenesis. In mice with adult-onset deletion of GIPR in oligodendrocytes, GIPR agonism fails to enhance the weight-loss effects of GLP-1R agonism. Mechanistically, GIPR agonism increases brain access of GLP-1R agonists, and GIPR signaling in oligodendrocytes is required for this effect. In addition, we show that vasopressin neurons of the paraventricular hypothalamus are necessary for the weight-loss response to GLP-1R activation, targeted by peripherally administered GLP-1R agonists via their axonal compartment, and this access is increased by activation of the GIPR in oligodendrocytes. Collectively, our findings identify a novel mechanism by which incretin therapies may function to promote synergistic weight loss in the management of excess adiposity.

INTRODUCTION

Glucose-dependent insulinotropic polypeptide (GIP) is a gut hormone released in response to the ingestion of glucose and fat. In addition to its well-described action on the incretin axis,[1] activation of the GIP receptor (GIPR) exerts pleiotropic metabolic benefits, which include improved lipid handling and storage,[2] appetite suppression, and weight loss through its action in the brain,[3] in particular when combined with long-acting glucagon-like peptide 1 receptor agonists (LAGLP-1RA).[4–6] Multi-receptor agonists engaging the GIPR and GLP-1R represent a significant advance in the pharmacological management of excess adiposity, producing substantial weight loss (>20%) in people with obesity, yet how GIPR activation signals in the brain to enhance the efficacy of GLP-1R agonism remains unclear.

The GIPR is expressed in discrete brain nuclei important to the regulation of energy homeostasis, including the mediobasal hypothalamus (MBH), which includes the median eminence (ME) and arcuate nucleus of the hypothalamus (ARH), and the area postrema in the hindbrain.[7] Following peripheral administration, fluorescently labeled GIPR agonists are detected almost exclusively in the ME, area postrema, and choroid plexus, ranking the ME and area postrema as top candidate brain sites mediating the central action of GIPR agonism.[8] Intriguingly, recent single-cell transcriptomics analysis revealed that the *Gipr* is enriched in the oligodendrocyte (OL) populations of the murine MBH and hindbrain[7,9–12] and human hypothalamus,[13] but how GIPR signaling affects OL biology, and whether this might contribute to the metabolic benefits associated with GIPR activation, is unknown. Although the area postrema is enriched in GIPR-expressing neurons, and GIPR agonism is believed to mediate its anti-aversive activity via this area of the brain,[8,14–16] the ME mostly contains non-neuronal cells, including a population of highly plastic OLs that constitutively turn over in adulthood and are responsive to acute and chronic nutritional and metabolic signals.[11,17]

Here, we used a combination of approaches to interrogate the role of the GIPR in adult OL biology and examine the contribution

of GIPR signaling in OLs to the weight-loss efficacy of GIPR and GLP-1R agonism in diet-induced obese mice. We provide evidence that the GIPR is expressed in myelinating OLs and enriched in OLs of the ME. OL-specific deletion of the GIPR in adulthood reduces adult oligodendrogenesis and OL survival in the ME, whereas treatment with GIPR agonists promotes ME oligodendrogenesis, supporting the functional relevance of GIPR activation in the regulation of OL and myelin plasticity in adult mice. We find that expression of the GIPR in OLs is required for GIPR agonism to enhance the weight-loss and appetite-suppressive effects of GLP-1R agonism. Mechanistically, GIPR agonism increases access of GLP-1R pharmacotherapies to the ME and ARH by increasing local VEGF-A expression and vessel fenestration, and GIPR expression in OL is required for GIPR agonism to enhance access of GLP-1R agonists to these regions. Collectively, our findings identify a novel mechanism by which GIPR/GLP-1R-based therapies may function via the GIPR to augment GLP-1R activation in the brain and promote synergistic weight loss, when compared with selective GLP-1R activation.

RESULTS

The *Gipr* is enriched in ME OLs

We first conducted a comprehensive evaluation of *Gipr* expression in OL lineage cells of the MBH, dorso-vagal complex (DVC), and main white matter tracts (corpus callosum [CC], optic nerve, amygdala, striatum, substantia nigra, VTA, and dorsal horn) in adult male mice, using multiplexed fluorescence *in situ* hybridization (FISH, RNAscope technology) against the *Gipr*, *Sox10*, *Pdgfra*, and *Plp1*. Consistent with published transcriptomics datasets,[7,9–11] we found very rare expression of the *Gipr* in OL progenitor cells (OPCs and *Sox10*$^+$/*Pdgfra*$^+$) across all examined regions (Figures 1A, 1B, and S1A). In contrast, the *Gipr* was present in OLs (*Sox10*$^+$/*Plp1*$^+$). The proportion of *Gipr*$^+$ OLs varied between regions and was significantly higher in the ME than the adjacent hypothalamic parenchyma (ARH) or all main white matter tracts (Figure S1B). To gain insights into the molecular identity of the subset of ME OLs expressing *Gipr*, we used our published single-cell transcriptomic dataset of the mouse murine ME[11] and analyzed genes differentially expressed between *Gipr*$^-$ and *Gipr*$^+$ OLs (Table S1). Top differentially expressed genes included *Klk6* and *Phlda1*, enriched in mature OLs[18]; *Marcks*, a regulator of OL maturation[19]; and interferon response gene *Ifi27l2a*, collectively suggesting an enrichment of the *Gipr* in mature myelinating OLs. Pathway analysis of genes enriched in *Gipr*$^+$ OLs revealed an enrichment in genes involved in adipogenesis and estrogen receptor signaling (Table S2). Next, we used a labeled GIPR agonist (GIPRA^{Cy5}) to examine the distribution of the GIPRA in the ME. Following intravenous administration, the GIPRA^{Cy5} was found in close proximity to SOX10$^+$ OL lineage cells in the ME. This indicates that peripherally dosed GIPR-based therapeutics are capable of targeting OLs in the MBH (Figure 1C).

Gipr expression is upregulated in ME OLs of diet-induced obese mice

In lean, healthy mice, the OL population in the ME turns over rapidly, with approximatively 50% being replaced within 6 weeks,[17] whereas high-fat (HF) feeding blunts ME OL turnover, leading to an accumulation of mature OLs in the ME.[17] Considering that the *Gipr* is enriched in mature OLs (Table S1), we evaluated whether diet-induced obesity (DIO) leads to an increase in the number of *Gipr*-expressing OLs in the ME. Consistent with our previous work, we found a 50% increase in ME OL density in mice maintained on a 60% HF diet when compared with age-matched chow-fed controls (average body weight 28.6 ± 1.6 vs. 48.8 ± 2.2 g) in chow and HF-fed mice, respectively (Figure 1D). This change was specific to the ME and not observed in any other inspected regions (ARH, NTS, AP, DMX, CC, optic nerve, amygdala, striatum, substantia nigra, VTA, or dorsal horn [not shown]). As predicted, DIO increased the number of OLs expressing the *Gipr* in the ME (Figure 1E) but not in other regions (Figures S1C and S1D).

GIPR signaling in OLs regulates adult ME oligodendrogenesis in HF-fed mice

To characterize the role of GIPR signaling in OLs during the development of DIO, we generated mice with adult-onset OL-specific *Gipr* deletion using *Plp1-CreER*^{T2} mice crossed with *Gipr*$^{fl/fl}$ mice[20] (OL$^{GIPR-/-}$) and wild-type (WT) littermates (OL$^{GIPR+/+}$). At post-natal day 60 (P60), mice received 8 daily intraperitoneal (i.p.) doses of tamoxifen (Tm, 80 mg/kg) to induce Cre expression in OLs and were switched to a 60% HF diet 2 weeks later. MBH micro-punches were collected at 3 and 15 weeks post Tm treatment to measure MBH *Gipr* expression. HF feeding produced a significant increase in MBH *Gipr* expression in OL$^{GIPR+/+}$ mice, consistent with RNAscope analysis (Figure 1E), which did not occur in OL$^{GIPR-/-}$ mice, resulting in a 40% reduction in MBH *Gipr* expression in OL$^{GIPR-/-}$ compared with OL$^{GIPR+/+}$mice (Figure S2A). FISH detection of *Gipr* in the ME of HF-fed OL$^{GIPR-/-}$ mice confirmed OL-specific deletion under these conditions (Figure S2C).

OL$^{GIPR-/-}$ and OL$^{GIPR+/+}$ were further crossed with a GFP reporter line (*R26-Yfp*) to label the OL population present at the time of Tm administration at P60 and measure the effect of *Gipr* knockout (KO) on ME OL lineage cell plasticity and longevity in mice maintained on a 60% HF diet (Figure S2B). In OL$^{GIPR-/-}$mice 12 weeks after Tm administration, there was a significant reduction in the density of OL lineage cells (SOX10$^+$) in the ME, with no change in the density of OPCs (SOX10$^+$/PDGFRa$^+$), suggesting a reduction in the density of OLs (Figures 2A and 2B). Further, we found a significant reduction in the density of both OLs present in the ME at the time of Tm administration (pre-existing OLs, SOX10$^+$/PDGFRa$^-$/YFP$^+$, Figures 2A and 2B) and OLs generated from OPC differentiation after Tm administration (new OLs, SOX10$^+$/PDGFRa$^-$/YFP$^-$, Figures 2A and 2B), suggesting that GIPR activation in OLs promotes OL longevity and adult oligodendrogenesis in the ME of HF-fed mice. Of note, because the *Plp1-CreER*^{T2} allele yields to 70% recombination,[17] the YFP$^-$ population also reflects OLs that did not undergo recombination. Consistent with a role for ME oligodendrogenesis in the maintenance of ME myelin in adulthood,[17] reduced oligodendrogenesis and longevity of ME OLs in OL$^{GIPR-/-}$ mice was associated with reduced expression of myelin basic protein (MBP) in the ME, a standard marker for visualizing myelin sheaths,[21] suggesting reduced myelination (Figures 2C and 2D). In contrast, the density of OL lineage cells was similar between groups in the CC (Figures S2D and S2E), indicating that responsiveness to peripheral GIPR activation is a feature of ME OLs.

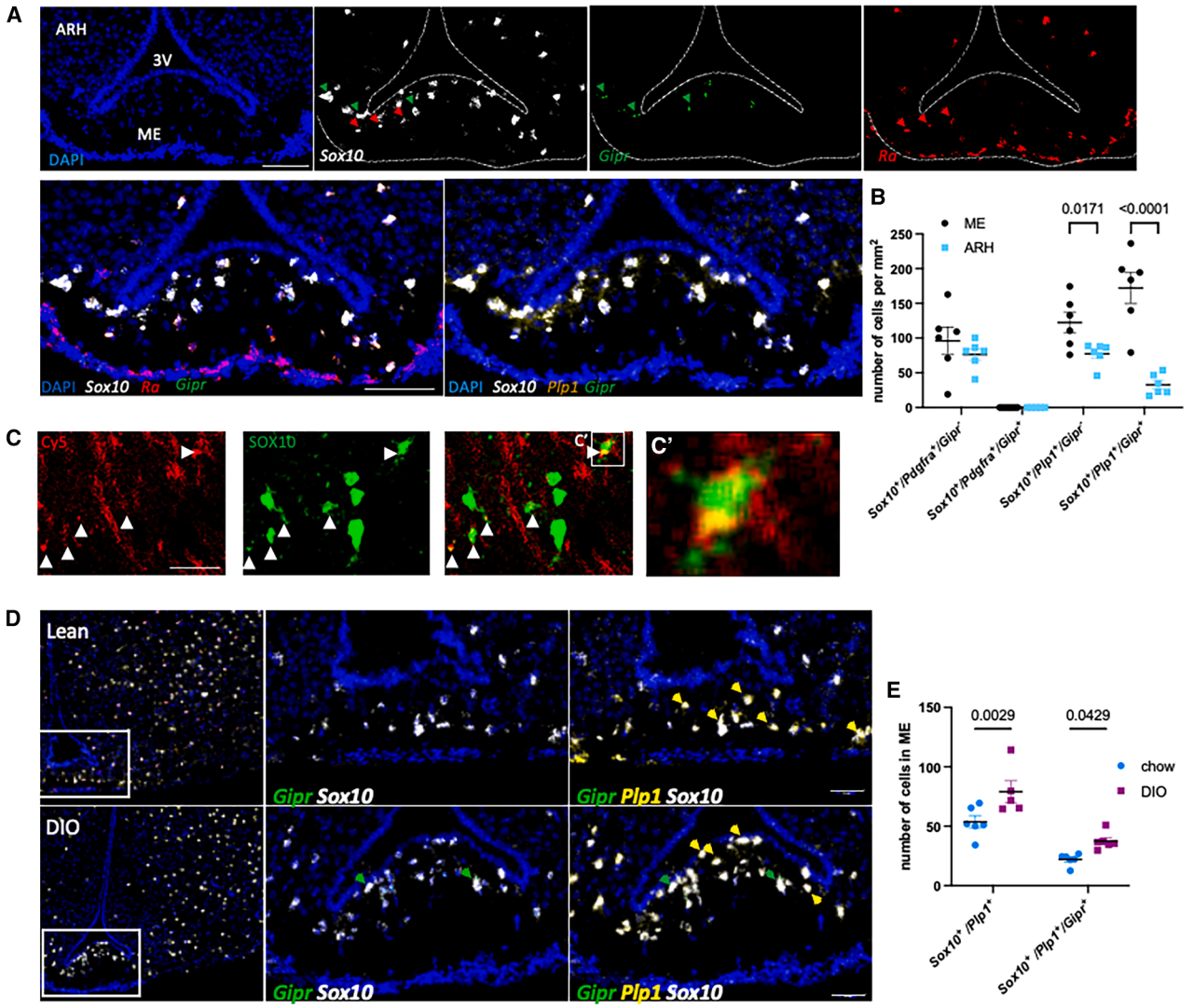

Figure 1. The *Gipr* is enriched in murine and human ME mature OLs

(A and B) Representative images (A) and quantifications (B) of FISH detection of *Gipr* (green) in oligodendrocyte lineage cells using *Sox10* to label the entire lineage (white), *Pdgfra* (Ra, red) to label OPCs (Sox10$^+$/Ra$^+$, red arrowheads), and *Plp1* (yellow) to label OLs in the mouse median eminence. *Gipr* expression OLs (*Gipr*$^+$/Sox10$^+$) are indicated by the green arrowheads. Each datapoint is the average of 3 sections per animal. Scale bar represents 50 μm.

(C) Immunofluorescent detection of the labeled GIPR agonist (GIPRA^{Cy5}, red) and colocalization with oligodendrocyte marker *Sox10* (green) in the mouse ME following intravenous administration. Scale bar represents 20 μm.

(D and E) Representative images (D) and quantification (E) of FISH detection of *Gipr* (green, green arrowheads) in oligodendrocyte lineage cells labeled with *Sox10* (white) and *Plp1* (yellow, yellow arrowheads) to label OLs in the mouse ME from mice fed a standard chow (lean) of 60% HF diet (DIO) for 8 weeks from P60. Each datapoint is the average of 3 sections per animal. Green arrowheads: *Gipr*$^+$ /*Sox10*$^+$ cells; yellow arrowheads: *Gipr*$^+$/*Sox10*$^+$/*Plp1*$^+$ cells. Scale bar represents 50 μm.

Data are presented as mean ± SEM and analyzed by Student's t test. See also Figure S1 and Tables S1 and S2.

GIPR signaling in OLs controls energy expenditure and insulin sensitivity in HF-fed mice

We next examined the metabolic phenotype of OL$^{GIPR\ -/-}$ mice maintained on a 60% HF diet. Body weight gain and body composition did not differ between OL$^{GIPR\ -/-}$ mice and WT littermates (Figures 3A and 3B). However, deletion of the GIPR in OLs significantly reduced energy expenditure and energy intake (Figures 3C–3E). Substrate utilization (RER, respiratory exchange ratio) and locomotor activity did not differ between groups (Figures S3A and S3B). OL$^{GIPR\ -/-}$ mice maintained glycemic control similar to OL$^{GIPR\ +/+}$ mice in response to an oral glucose challenge (Figure 3F) but had impaired insulin tolerance following an i.p. dose of insulin bolus (Figure 3G), suggesting impaired insulin sensitivity. No significant changes were found in liver and epididymal white adipose tissue (eWAT) cellularity (Figures S3C and S3D), but there was a trend toward larger adipocytes in the interscapular brown adipose tissue (iBAT) and increased lipid droplet area in the iBAT of OL$^{GIPR-/-}$ mice (Figure 3H). Metabolomics analysis of plasma and tissue samples from OL$^{GIPR-/-}$ and OL$^{GIPR+/+}$ mice using multivariate

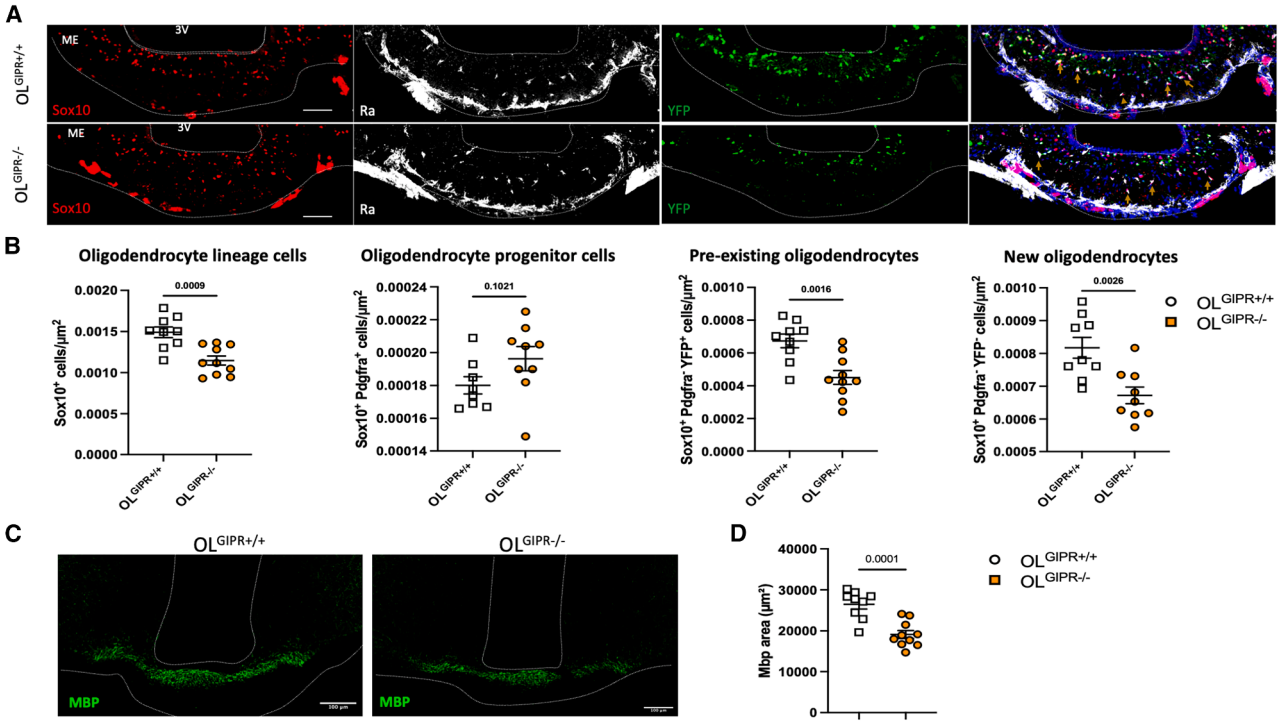

Figure 2. GIPR signaling in OLs regulates ME oligodendrogenesis in HF-fed mice

(A and B) Representative images (A) and quantification (B) of oligodendrocyte lineage cells labeled with YFP at P60 for fate-mapping purposes and detected using multiplexed immunofluorescent detection of SOX10 (red), PDGF receptor agonist (Ra, white), and YFP (green) in the ME of HF-fed $OL^{GIPR\ +/+}$ and $OL^{GIPR\ -/-}$ mice. Scale bar represents 50µm. Yellow arrow heads show OPCs, coexpressing *Sox10* and *Pdgfra*.

(C and D) Representative images (C) and quantification (D) of MBP (green) in the ME of HF-fed $OL^{GIPR\ +/+}$ and $OL^{GIPR\ -/-}$ mice. Scale bar represents 100 µm. Data are presented as mean ± SEM and analyzed by Student's t test. See also Figure S2.

analysis of variance (MANOVA) indicated clear group segregation of the overall metabolite profile (Figure S3E, Table S3). Univariate statistical analysis highlighted changes in concentrations of circulating and tissue amino acid and related metabolites' concentrations, in particular metabolites involved in branched chain amino acid (BCAA) metabolism, such as isovalerylcarnitine, beta-hydroxyisovaleric acid, N-acetylleucine, 3-methyl-2-oxovaleric acid, 2-hydroxyisocaproic acid, or 3-hydroxyisobutyric acid, all of which decreased in the adipose tissue of $OL^{GIPR-/-}$ mice ($p < 0.05$ in eWAT, $p < 0.1$ in iBAT) (Figure S3F, Table S3). Consistently, correlation network analysis[22] highlighted significant changes in BCAA metabolism in $OL^{GIPR-/-}$ compared with WT mice (Table S3). Thus, despite the lack of a net effect on body weight, these data support a role for endogenous GIPR signaling in OLs in the regulation of whole-body energy homeostasis, glycemic control, and BCAA utilization in HF-fed mice.

GIPR agonism promotes ME oligodendrogenesis and OL turnover

GIPR agonism has emerged as an effective therapeutic strategy in the metabolic field, through its ability to potentiate the appetite- and weight-lowering action of GLP-1R agonism. However, the underpinning mechanisms are incompletely understood. To determine whether GIPR agonism mediates its therapeutic activity via ME OLs, we examined the consequences of treatment with a long-acting GIPR agonist (LAGIPRA, 300 nmol/kg[23]) in *Opalin-iCreER^{T2}:TdTom* male mice. In these mice, Tm administration at P60 induces TdTom expression specifically in mature OLs, allowing us to quantify OL survival and new OL production.[23] Mice were dosed with the LAGIPRA for 2 weeks shortly after Tm administration on chow maintenance, following 8 weeks on a 60% HF diet to induce DIO (Figures S4A and S4B).

In chow-fed lean mice, GIPR agonism did not significantly impact weight gain (Figure S4C) but significantly increased the number of OL lineage cells in the ME, with both an increase in OPC and OL density over 2 weeks (Figures S4E and S4F). We measured both an increase in the number of OLs labeled with TdTom, indicating increased survival of ME OLs, and an increase in $TdTom^-$ OLs, indicating increased oligodendrogenesis (Figures S4E and S4F). Consistent with these changes, ME MBP immunolabeling increased in mice dosed with the LAGIPRA (Figures S4G and S4H). Thus, GIPR agonism increases oligodendrogenesis and OL survival in the ME in lean chow-fed mice (Figure S4K).

In DIO mice, chronic treatment with the LAGIPRA produced a modest but significant decrease in body weight (Figure S4D). As previously reported, DIO significantly increased ME OL density,[17] but this response was blunted in the LAGIPRA-treated mice (Figures 4A and 4B). Because OL density results from both oligodendrogenesis and OL turnover in the ME,[17] we used complementary approaches to quantify both processes.

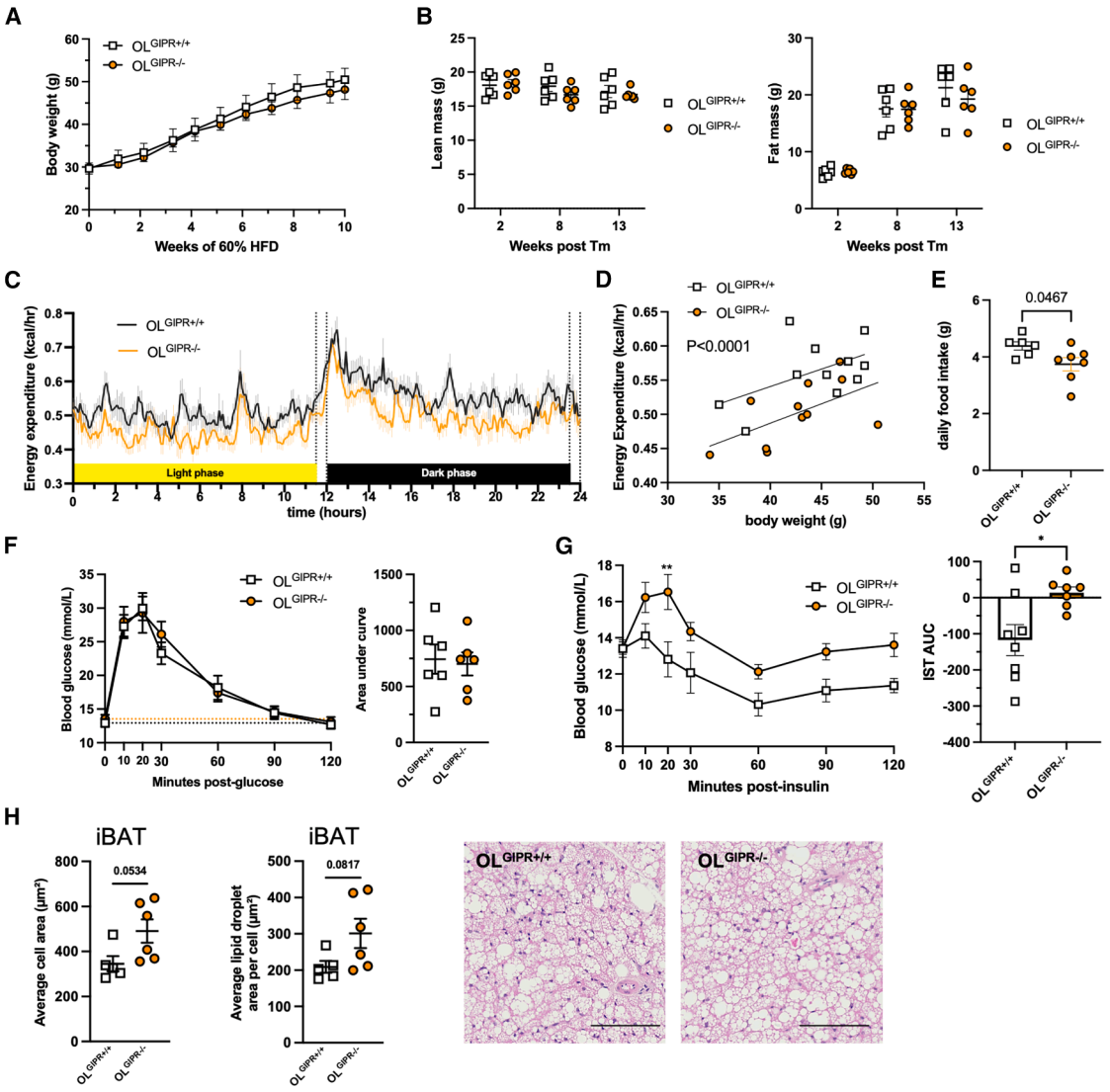

Figure 3. GIPR signaling in OLs regulates energy expenditure and insulin sensitivity in HF-fed mice

Body weight gain (A), body composition (B), energy expenditure (C), correlation between energy expenditure and body weight (D), energy intake (E), blood glucose excursion during an oral glucose tolerance test (F) or i.p. insulin tolerance test (G), and cellularity analysis of iBAT adipocytes (H) in the metabolic phenotyping cohort of $OL^{GIPR\ -/-}$ and $OL^{GIPR\ +/+}$ mice maintained on 60% HF diet. Scale bar represents 50 μm.

Data are presented as mean ± SEM and analyzed by 2-way ANOVA (A–G) or Student's t test (H). See also Figure S3 and Table S3.

The proportion of newly formed OLs was increased following LAGIPRA treatment, suggesting increased oligodendrogenesis (Figures 4A and 4B). This was accompanied by a decrease in OPC density and an increase in the density of $Edu^+/Pdgfra^-/Sox10^+$ cells following a 24-h EdU pulse at the end of the 2-week treatment, suggesting rapid differentiation of recently divided OPCs (Figures 4E and 4F). In addition, 2 weeks of treatment with the LAGIPRA increased the number of OL lineage cells expressing *Bmp4*, a specific marker for newly formed OLs,[24] specifically in the ME, further indicating that GIPR agonism in DIO mice increases oligodendrogenesis (Figures S4I and S4J). We also observed an increase in the density of BCAS1, a specific marker of early-myelinating OLs[25] under these conditions (Figures 4G and 4H). Moreover, in the fate-mapping study, we measured a decrease in the density of $TdTom^+$ pre-existing OLs (Figures 4A and 4B) with GIPR agonism, indicating increased OL turnover. As a result of both an increase in oligodendrogenesis and an increase in OL turnover, MBP density was similar between groups (Figures 4C and 4D). Thus, GIPR agonism promotes ME oligodendrogenesis in DIO mice and restores OL turnover (Figure 4I).

GIPR signaling in OLs is required for GIPR agonism to enhance the weight-loss efficacy of GLP-1R agonism in obese mice

Based on our previous finding that adult OL plasticity regulates hypothalamic leptin sensing,[17] we hypothesized that GIPR-agonist-induced changes in ME OL turnover in DIO mice might

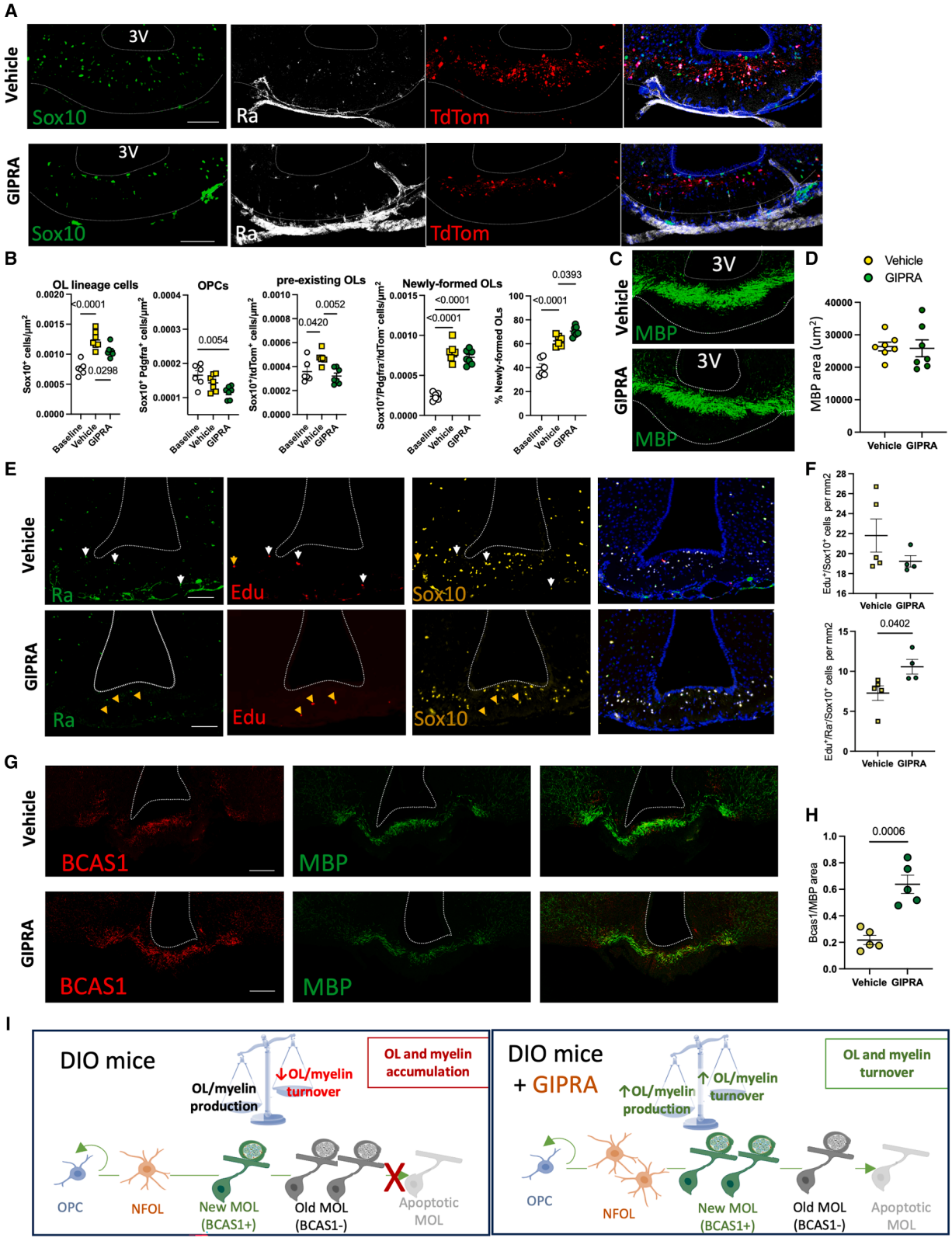

(legend on next page)

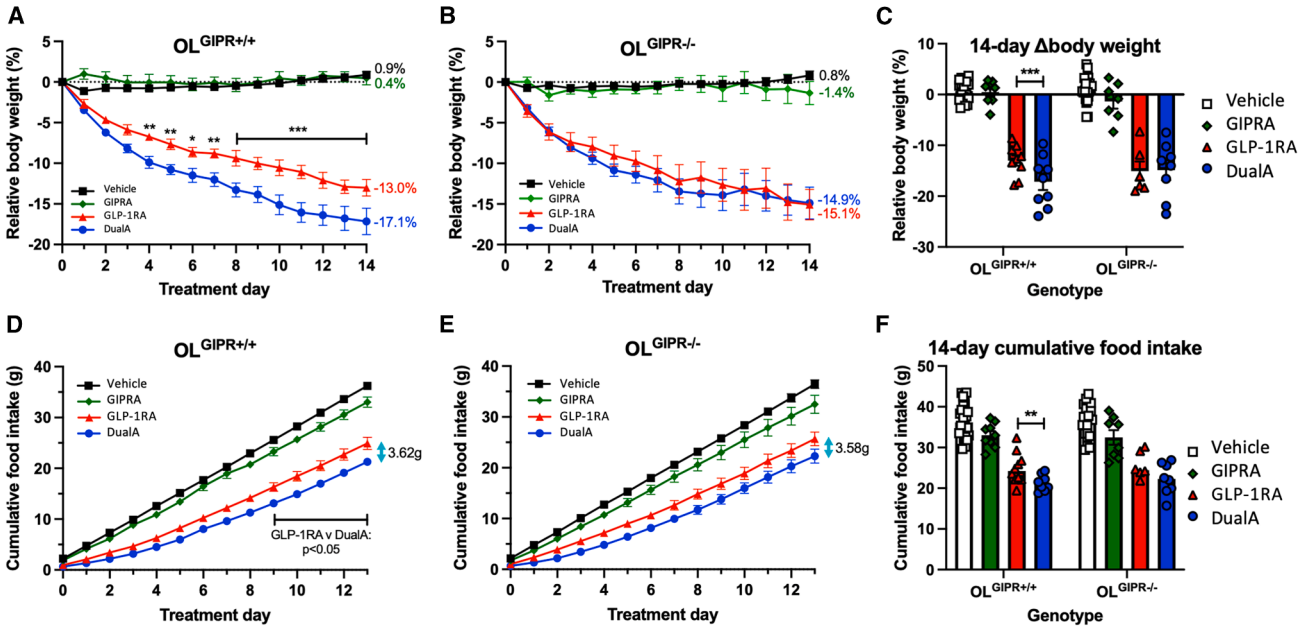

Figure 5. GIPR signaling in OLs is required for the beneficial effects of GIPR agonism the anti-obesity actions of GLP-1R agonist

(A–C) Body weight change in $OL^{GIPR+/+}$ (A and C) and $OL^{GIPR-/-}$ (B and C) mice in response to vehicle, LAGIPRA, LAGLP-1RA, and combination (DualA) treatments as a proportion of baseline body weight (n = 7–9).

(D–F) Cumulative food intake in $OL^{GIPR+/+}$ (D and F) and $OL^{GIPR-/-}$ (E and F) mice in response to vehicle, LAGIPRA, LAGLP-1RA, and combination (DualA) treatments.

Data presented as mean ± SEM. GIPR agonism vs. GLP-1R agonism $p^{*} < 0.05$, ** < 0.01, *** < 0.001, **** < 0.0001. GIPR agonism vs. DualA $^{\$\$} < 0.01$, $^{\$\$\$} < 0.001$, $^{\$\$\$\$} < 0.0001$. GLP-1R agonism vs. DualA $p^{\#} < 0.05$, $^{\#\#} < 0.01$.

Data presented as mean ± SEM and analyzed with a 2-way ANOVA (A, B, D, and E) or 1-way ANOVA (C and F). See also Figure S5.

alter hypothalamic sensing of metabolic signals. If true for hypothalamic sensing of GLP-1R agonists, this might represent a novel mechanism by which GIPR activation enhances the weight-loss benefits of GLP-1R agonism. To explore this possibility, we first examined the role of OL GIPR signaling in the weight-loss action of combined GIPR and GLP-1R agonism.

$OL^{GIPR\ -/-}$ mice and WT littermates were maintained on a 60% HF diet for 10 to 16 weeks to reach an average body weight of 45 g. Mice were then dosed subcutaneously with a vehicle for 2 weeks, followed by daily treatment with either a LAGLP-1RA alone or in combination (DualA) with the LAGIPRA (Figure S5A). Again, $OL^{GIPR\ -/-}$ mice gained a similar amount of body weight as controls during HF diet maintenance (Figure S5B). In WT controls, treatment with the LAGLP-1RA significantly reduced body weight and food intake, which were amplified by the LAGIPRA (Figures 5A, 5C, 5D, and 5F). In contrast, in $OL^{GIPR-/-}$ mice, the LAGIPRA failed to augment the anorectic or weight-loss profile of the LAGLP-1RA (Figures 5B, 5C, 5E, and 5F). Thus, our findings suggest that GIPR signaling in OLs is required for GIPR agonism to enhance the anti-obesity efficacy of GLP-1R agonism in HF-fed obese mice.

GIPR signaling in OLs increases access of a peripherally dosed LAGLP-1R agonist to the MBH

Adult-born OLs have been recently shown to modulate hypothalamic neuroendocrine functions in response to hormonal and nutritional signals by regulating the expression of the angiogenic factor VEGF-A, enhancing ME vascular permeability.[26,27] Based on these findings, we hypothesized that the upregulation of new OL production in response to GIPR agonism might increase vascular permeability at the ME-ARH barrier and enhance the access of circulating molecules to their hypothalamic targets. This could be specifically relevant during co-treatment with GLP-1R agonists, which do not cross the blood-brain barrier.[28]

Figure 4. GIPR agonism increases ME oligodendrogenesis and oligodendrocyte turnover

(A–D) Representative images (A and C) and quantification (B and D) of the immunoreactivity against SOX10 (green), PDGF receptor agonist (Ra, white), TdTom (red), and MBP (green) in the ME of HF-fed *opalin-iCreER^{T2}:TdTom* mice following Tm administration at P60 and 2 weeks of subcutaneous daily dosing with a long-acting GIPR agonist or vehicle. Scale bar represents 100 μm.

(E and F) Representative images (E) and quantification (F) of the immunoreactivity against SOX10 (yellow), PDGF receptor agonist (Ra, green), and Edu (red) in the ME of HF-fed mice following 2 weeks of subcutaneous daily dosing with a long-acting GIPR agonist or vehicle and 4 doses of intraperitoneal EdU over 24 h just before terminal perfusion. Scale bar represents 100 μm.

(G and H) Representative images (G) and quantification (H) of the immunoreactivity against BCAS1 (red) in the ME of HF-fed mice following 2 weeks of subcutaneous daily dosing with a long-acting GIPR agonist or vehicle. Scale bar represents 100 μm.

(I) Summary schematic of the effect of GIPR agonism on the ME oligodendrocyte lineage in DIO mice.

Data are presented as mean ± SEM and analyzed with Student's t test. See also Figure S4.

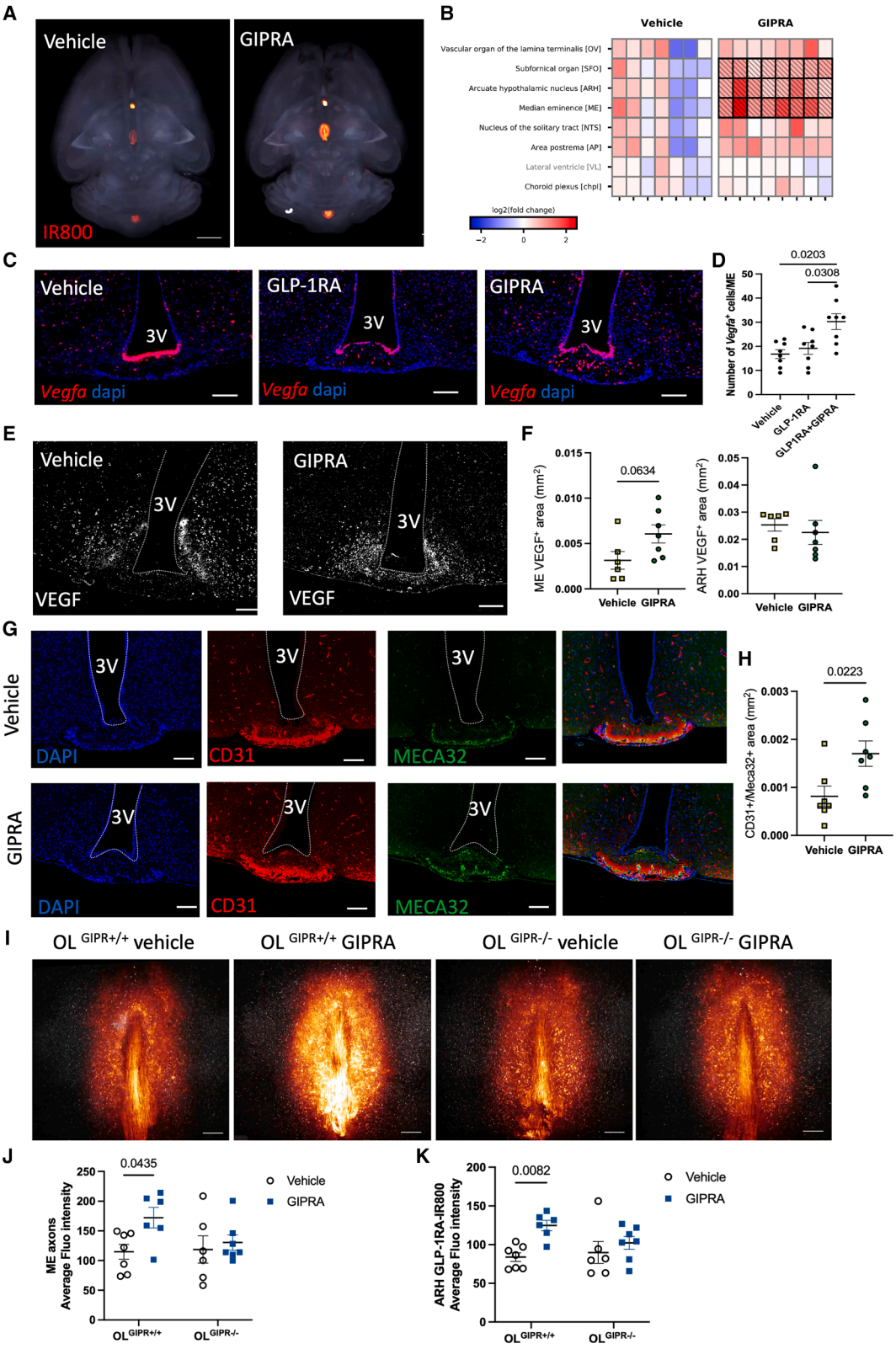

Figure 6. GIPR signaling in OLs increases access of a peripherally dosed LAGLP-1R agonist to the MBH

(A and B) Representative images (A, scale bar represents 1 mm) and quantification of the fluorescence intensity compared with mean intensity in the vehicle group for each brain region (B) of the brain distribution of IR-800 imaged at low resolution in WT mice following a pre-treatment with vehicle or GIPR agonism for 7 days

(legend continued on next page)

Using brain clearing and light-sheet microscopy to visualize the distribution of a fluorescently labeled short-acting GLP-1R agonist (SAGLP-1RA, Exendin-4) following peripheral administration, we found that peripherally administered GLP-1R agonists selectively access the brain through circumventricular organs, with the ME being one of the top brain regions exposed to peripherally administered GLP-1R agonists, consistent with the published literature[29,30] (Figures S6A and S6B; Videos S1 and S2).

To test this hypothesis, DIO C57/Bl6J males were treated for 6 days with the LAGIPRA or vehicle and on the day of sacrifice injected with a single dose of SAGLP-1RA^{IR800} subcutaneously. Brains were collected and processed for clearing and fluorescent light-sheet microscopy. Treatment with the GIPR agonist significantly increased IR800 fluorescence in the ME, ARH, and subfornical area but not in other circumventricular organs (Figures 6A and 6B). Thus, GIPR activation increases hypothalamic access of GLP-1R agonists. Consistent with a change in ME-ARH vascular permeability, we found an increase in the number of cells expressing *Vegfa* specifically in response to GIPR but not GLP-1R agonism (Figures 6C and 6D). This was associated with an increase in the area immunoreactive for VEGF (Figures 6E and 6F) and an increase in the density of MECA32^{+} fenestrated capillaries under these conditions (Figures 6G and 6H).

We tested the role of GIPR signaling in OL in the increased brain access of GLP-1RA following GIPR activation. Tm-dosed OL$^{GIPR-/-}$ mice and WT littermates were maintained on a 60% HF diet for 12 to 16 weeks to reach a minimum body weight of 45 g, followed by 7 daily subcutaneous injections with a LAGIPRA or vehicle (Figures S6C and S6D). On the day following the last dose, all mice received a single intravenous dose of SAGLP-1RA^{IR800} and brains were collected and processed for clearing and fluorescent light-sheet microscopy of the MBH at high resolution. In WT mice, 7 days pre-treatment with the LAGIPRA significantly increased IR800 fluorescence intensity in the ME and ARH (Figures 6I–6K). In contrast, in OL$^{GIPR-/-}$ mice, there was no effect of the LAGIPRA on the uptake of the labeled GLP-1RA in the ME and ARH (Figures 6I–6K). Taken together, our findings indicate that GIPR agonism increases vascular permeability in the ME of DIO mice, facilitating brain access of GLP-1R agonists, and that GIPR signaling in ME OLs is required to increase the uptake of GLP-1RA-based therapeutics in the MBH.

PVH AVP neurons access peripherally administered GLP-1R agonists through their axonal segment in the ME, enriched in GLP-1R

In WT mice, ME uptake of the SAGLP-1RA^{IR800} was specifically high in fiber bundles oriented in the rostro-caudal axis (Figures 6I and 6J; Video S2; 7A and 7B, white arrow), reminiscent of myelinated magnocellular axonal tracks that travel across the dorsal ME to project to the posterior pituitary[11,31] (Figure 7C). Confocal imaging of thin sections from these brains confirmed that SAGLP-1RA^{IR800} colocalizes with MBP (Figures 7D and 7D′), indicating that peripherally dosed GLP-1R agonists accumulate alongside ME myelinated axons. We obtained further evidence of the neurochemical identity of ME myelinated axons using high-resolution microscopy to colocalize arginine vasopressin (AVP) with MBP and confirmed that vasopressin axons are myelinated, at least in their ME segments (Figure 7E).

Intriguingly, recent transcriptomic findings from the mouse and human hypothalamus indicate that PVH vasopressin neurons are highly enriched in GLP-1R transcript,[9,13] raising the possibility that peripherally dosed GLP-1R agonists might access PVH GLP-1R^{+} neurons through their axonal segments in the ME. To confirm this, we used super resolution microscopy to characterize the expression of the GLP-1R in ME myelinated axons. GLP-1R immunolabeling overlapped with MBP AVP and CASPR, a protein specifically expressed at nodes of Ranvier, (Figures 7F and 7G, S7A). This indicates that the GLP-1R is expressed in the ME, within myelinated axons of magnocellular AVP neurons. Thus, the axonal segment of magnocellular AVP neurons in the ME is a direct target of peripherally dosed GLP-1R agonists.

PVH vasopressin neurons are required for the weight-loss efficacy of GLP-1R agonists

The ME portion of PVH GLP-1R^{+} axons, which is specifically exposed to GLP-1R agonists after peripheral dosing, might represent a functionally relevant site for GLP-1R agonists to exert their weight-loss effects. To test this, 9-week-old *Avp-Cre* or WT littermates were injected in the PVH with AAV particles expressing Cre-inducible hM4Di (PVH^{AVPGi} and PVH^{AVP-WT}, respectively), a designer receptor exclusively activated by designer drugs, allowing inducible inhibition of PVH vasopressin neurons with deschloroclozapine (DCZ), a potent and selective chemogenetic activator.[32] Immunodetection of the co-expressed RFP reported confirmed spread of the virus throughout the PVH (Figure S7B). Three weeks post viral hM4Di injection,

and a terminal bolus with IR800-Ex4. In (B), each column represents the fluorescence intensity in 1 individual brain sample. Fluorescence intensity for every animal in the GIPR-treated group is compared with the mean value in the vehicle-treated group and represented as a heatmap. Areas showing statistically significant compound fluorescence intensity changes are highlighted in hashed and bold.

(C and D) Representative images (C) and quantification (D) of FISH detection of *Vegfa* (red) in the ME of DIO mice treated for 7 days with a GLP-1RA alone or in combination with the GIPRA.

(E and F) Representative images (E) and quantification (F) of VEGF immunodetection in the ME of DIO mice treated for 7 days with the GIPRA.

(G and H) Representative images (G) and quantification (H) of CD31 (red) and MECA32 (green) immunodetection in the ME of DIO mice treated for 7 days with the GIPRA. Scale bar represents 100 μm.

(I–K) Representative images of a ventral view of IR-800 fluorescence in the MBH, imaged with fluorescent light-sheet microscopy at high resolution (I, scale bar represents 200 μm), and quantification of IR800 fluorescence in fibers of the ME (J) and adjacent ARH region (K) in HF-fed OLGIPR$^{-/-}$ mice and WT littermates following a pre-treatment with vehicle or GIPR agonism for 7 days and a terminal bolus with IR800-Ex4.

Data are presented as mean ± SEM (n = 6–7) and analyzed with a negative binomial generalized linear model with Tukey's test as post hoc analysis to determine differential signal accumulation between groups with false discovery rate (FDR) correction (<0.05) (B), Student's t test (D, F, and H) or 2-way ANOVA (J and K). See also Figure S6.

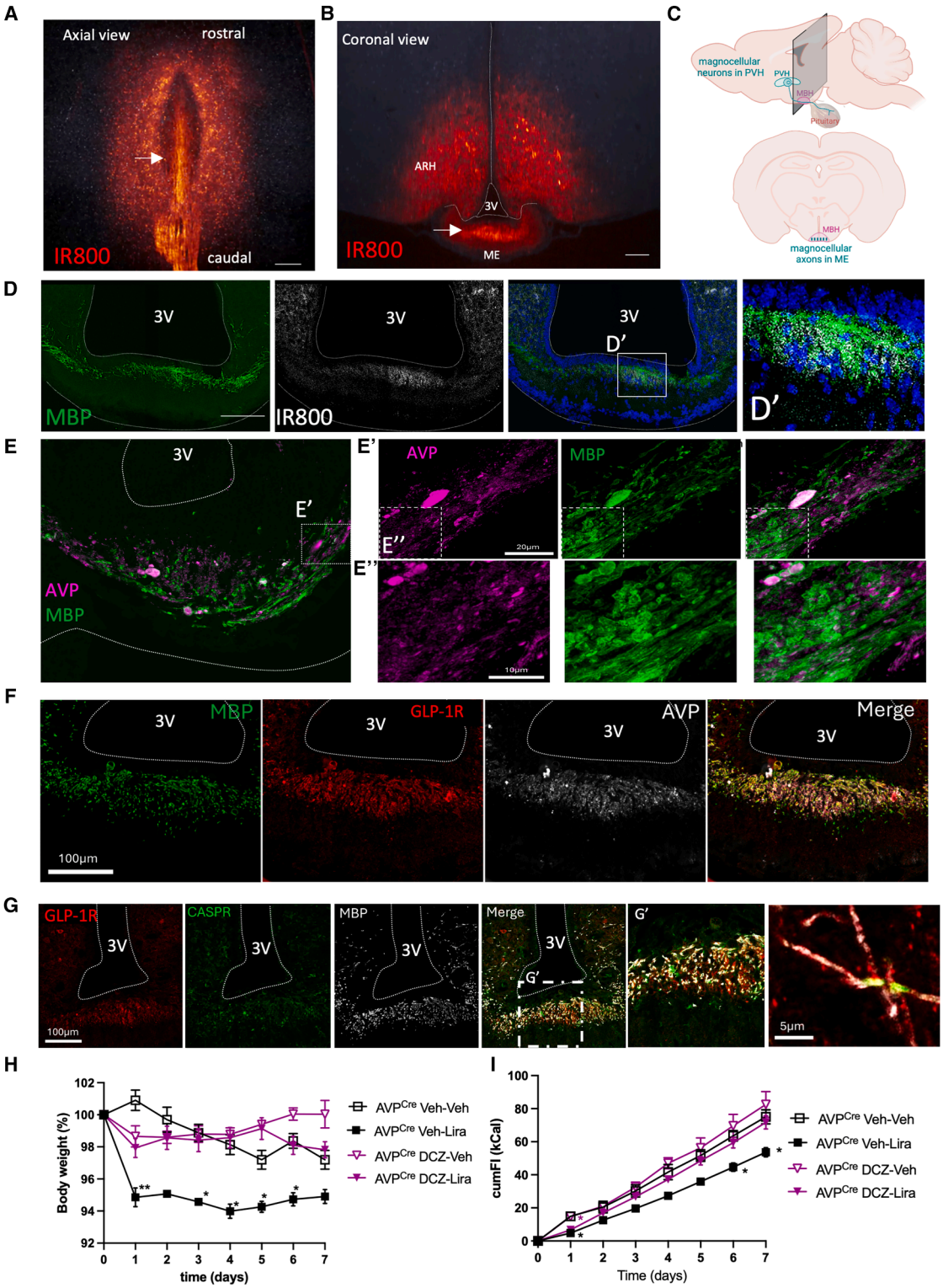

Figure 7. PVH AVP neurons are required for the weight-loss response to GLP-1R agonism and access peripherally administered GLP-1R agonists through their axonal segment in the ME

(A and B) Ventral view (A) and coronal view (B) of the MBH of a cleared brain from a mouse injected intravenously with IR-800 GLP-1R and imaged at high resolution with light-sheet microscopy, visualized in glow scale and autofluorescence in gray. White arrows indicate myelinated axon bundles.

(C) Schematic representation of the orientation of PVH magnocellular axons.

(legend continued on next page)

mice were split into 2 groups, treated either with DCZ or its vehicle (DMSO) via the drinking water. After 3 weeks of DCZ or DMSO treatment, mice were dosed subcutaneously with vehicle for 7 days, followed by a 7-day treatment with a LAGLP-1RA (liraglutide). Body weight and food intake did not vary between *Avp-Cre* mice and WT littermates following hM4Di injection and DCZ or DMSO treatment through the drinking water (data not shown). Likewise, food intake and weight gain remained similar between groups during vehicle treatment. Treatment with the LAGLP-1RA significantly reduced appetite and body weight in control $PVH^{AVP\text{-}WT}$ mice treated with either DMSO or DCZ, confirming that DCZ treatment itself does not affect these responses. PVH^{AVPGi} mice receiving DMSO through the drinking water also exhibited the expected appetite-suppressing effect and weight loss in response to LAGLP-1RA treatment (Figures 7H, 7I, S7C, and S7D). In contrast, the LAGLP-1RA failed to produce weight loss and reduce food intake in PVH^{AVPGi} mice receiving DCZ through the drinking water (Figures 7H and 7I). Thus, PVH vasopressin axons, which access peripherally dosed GLP-1R agonists via their axonal segment in the ME, are required for the weight-loss response to GLP-1R agonism.

Discussion

The anti-obesity effect of GIPR agonism occurs primarily via the brain,[3] yet our understanding of how central activation of the GIPR modulates the neural circuits orchestrating energy homeostasis, and augments weight loss elicited by GLP-1R agonism, remains incomplete. Here, we show that *Gipr* is expressed in white matter OLs and enriched in OLs of the ME, highlighting the need to characterize the role of OLs in the central action of GIPR activation.

A major finding of our studies is that GIPR signaling bidirectionally regulates oligodendrogenesis in the adult ME. This conclusion is supported by the decrease in new OL production measured in the ME following OL-specific *Gipr* deletion. Conversely, GIPR agonism leads to an increase in the density of *Bmp4*$^+$ and BCAS1$^+$ OLs, two markers specifically expressed in newly formed and early-myelinating OLs.[24,25] Consistent with an increase in oligodendrogenesis, genetic fate mapping studies indicate an increase in the proportion of unlabeled OLs (Sox10$^+$/Pdgfra$^-$/TdTom$^-$) in mice treated with the GIPR agonist. Since the GIPR is not expressed in OPCs, this suggests an indirect effect of GIPR activation on OPC differentiation and/or the survival of newly formed OLs. Previous studies have identified a number of signaling molecules secreted by myelinating OLs to regulate proliferation and differentiation of local OPCs, for example, PDGFA.[33,34] Alternatively, changes in the survival of mature OLs can affect OPC proliferation and differentiation through changes in local myelin debris production, which is a strong regulator of OPCs differentiation.[35] The increased proportion of Pdgfra$^-$/Brdu$^+$/Sox10$^+$ cells in the ME of GIPRA-treated mice following 24 h Brdu labeling further indicates that activation of the GIPR promotes rapid differentiation (loss of PDGFRa expression) of recently divided progenitors but does not affect proliferation.

Although our results indicate increased oligodendrogenesis in response to GIPR agonism in both lean and obese mice, the consequences on OL longevity differ, leading to a difference in the net effect on ME OL and myelin density. In lean mice, GIPR agonism increases ME OL survival, leading to a robust increase in OL density and MBP density, a proxy for myelination. This is remarkable because OL and myelin density in the ME are normally tightly regulated, despite continuous production of new myelinating OLs.[17] Together with our data indicating reduced OL survival and MBP density following deletion of the GIPR in OLs, these findings support the conclusion that GIPR signaling in OLs regulates OL and myelin longevity in the ME. A pro-survival role for GIP-GIPR signaling pathways has been previously reported in pancreatic beta cells through T cell-specific transcription factor (TCF) signaling.[36] Shared intracellular mechanisms might be engaged in OLs, which require TCF7l2 for differentiation and survival.[37] In contrast, treatment with the GIPR agonist in obese mice promotes OL turnover, suggesting the contribution of distinct cellular pathways in this pathological context. Given the crucial role played by microglia under normal conditions to maintain EM OL and myelin turnover,[17] this could reflect an impaired phenotype of local phagocytes in the inflamed hypothalamus of DIO mice.[38] Continuous turnover is a normal feature of ME OLs in adult healthy mice,[17] and although its functional relevance remains to be fully characterized, evidence so far indicates that it benefits energy balance regulation by promoting hypothalamic leptin sensitivity and systemic glucose homeostasis.[17,27] Thus, the increase in OL turnover during GIPR agonism may help restore blunted OL plasticity in DIO mice, which is a beneficial outcome. These findings highlight the need to investigate the mechanism of action of GIPR-based therapeutics in the obese state, where incretin receptor agonism might engage different pathways.

The consequences of HF feeding on OL lineage cells are specific to the ME and not observed in white matter tracts such as the CC.[17] Likewise, OL and myelin turnover, as well as nutritional regulation of OPC differentiation occur specifically in the ME.[11] Privileged access to unbuffered circulating factors, including GIPRAs,[8] might create a local niche in the ME promoting this unique plasticity.

Considering that whole-body KO of the GIPR confers resistance to DIO, we examined the potential contribution of GIPR

(D) Immunodetection of MBP and imaging of IR800 fluorescence in the MBH of a mouse injected intravenously with $SAGLP\text{-}1RA^{IR800}$. Scale bar represents 100 μm.
(E and E″) Immunodetection of MBP (green) and AVP (magenta) in the mouse MBH imaged with super resolution microscopy at 63X.
(F) Immunodetection of GLP-1R (red), AVP (white), and MBP (green) imaged with super resolution microscopy at 63X. Scale bar represents 100 μm.
(G) Immunodetection of GLP-1R (red), MBP (white), and CASPR (green) imaged with super resolution microscopy at 63X. Scale bar represents 100 μm.
(H and I) Body weight loss (H) and cumulative food intake (I) in Avp-Cre mice injected with AAV particles expressing hM4Di in the PVH and treated with either DCZ (DCZ PVH^{AVPGi}, $n = 6$) or vehicle (DMSO, DMSO PVH^{AVPGi}, $n = 6$) and receiving a daily subcutaneous injections with LAGLP-1RA (Lira) or vehicle for 7 days.
*: $p < 0.05$ Lira vs. vehicle.
Data presented as mean ± SEM and analyzed with 3-way ANOVA. See also Figure S7.

signaling in OLs. As observed following brain-wide *Gipr* deletion,[3] loss of the *Gipr* in OLs reduces energy intake, but this decrease is compensated by a reduction in energy expenditure, with no change in body weight. Thus, deletion of the GIPR specifically in OLs does not lead to the protection against DIO observed following brain-wide GIPR deletion. In contrast, unlike brain-wide GIPR deletion, lack of the GIPR in OLs led to an altered responsiveness to a peripheral insulin bolus, independently of body weight and body composition. This effect is likely mediated by changes in peripheral substrate utilization and storage, increased lipid deposition in BAT, and a dysregulated BCAA metabolism in $OL^{GIPR-/-}$ mice.[39–41] These results highlight the pleiotropic consequences of adult OL plasticity on systemic metabolism and its contributions to the metabolic consequences of GIPR agonism.

Although GIPR agonism enhances the weight-loss efficacy of GLP-1R agonism in preclinical models of obesity and adult humans with type 2 diabetes, the mechanisms by which activation of GIPR functions improves the outcome of GLP-1R signaling in the brain remain to be elucidated. Importantly, transcriptomics studies have failed so far to identify a candidate appetite-suppressing cell population co-expressing the GIPR and GLP-1R, *a fortiori* in brain areas accessed by incretin-based therapeutics,[8,29] suggesting a multi-cellular mode of action.[7,9,10] Most studies aiming to elucidate the mechanism through which GIPR agonism improves the efficacy of GLP-1R agonists have focused on identifying the neuronal populations and/or downstream circuits promoting the synergistic appetite suppression. GABAergic neurons of the area postrema[15,42] have been proposed to contribute by attenuating the aversive response to GLP-1R agonism. Further, brain-wide deletion of the GIPR in GABA-ergic neurons suppresses the potentiating action of GIPR agonism on the weight-loss response to GLP-1R agonism.[16] As expected, deletion of the GIPR in GABAergic neurons blunts neuronal activation in the area postrema following treatment with a GIPR agonist.[16] However, other GABA-ergic GIPR-expressing populations, such as in the hypothalamus,[7] might also contribute to this phenotype. Here, we propose that activation of the GIPR in OLs contributes to the synergistic weight loss provide by incretin-based multi-receptor agonists. Our results provide evidence that differential brain access to relevant GLP-1R target sites—here, the GLP-1R-expressing cell compartments of the ME—is a mechanism through which GIPR agonism can enhance the weight-loss efficacy of GLP-1R agonists. We show that GIPR agonism increases the expression of *Vegfa* and VEGF in the ME of HF-fed mice. VEGF is a well-known potent inducer of vascular hyperpermeability.[43,44] In the ME, VEGF expression has been shown to upregulate ME-ARH barrier permeability and hormone access through the regulation of local vessel fenestration.[45,46] Consistently, we observed an increase in the density of fenestrated capillaries in the ME of mice treated with GIPRA. Our data convincingly show that increased diffusion of the fluorescently labeled GLP-1R agonist in the ME-ARH requires activation of the GIPR in OLs. We propose that the increase in new OL production following GIPRA treatment regulates barrier function in response to GIPR agonism. In fact, newly formed OLs have been recently implicated in the regulation of vascular permeability in the ME through the regulation of VEGF-A expression.[26,27] Collectively, these data support the conclusion that GIPR signaling in OLs increases the permeability of the ME-ARH barrier and may facilitate increased access of incretin therapies to anorectic neuronal populations expressing the GLP-1R.

A key finding of our studies is that PVH^{AVP} neurons are implicated in the weight-loss efficacy of systemic GLP-1R agonism. This finding is particularly noteworthy given recent reports indicating that PVH^{AVP} neurons represent one of the neuronal populations with the highest GLP-1R enrichment in the mouse and human hypothalamus.[9,13] Importantly, a role for PVH^{AVP} neurons in the control of food intake and the long-term regulation of body weight is highlighted by numerous studies in preclinical models of obesity.[47–50] Further, $PVH^{Glp\text{-}1r}$ neurons are important for the control of acute feeding behavior and energy homeostasis.[51,52] However, our results contrast with the lack of effect of acute chemogenetic inhibition of $PVH^{Glp\text{-}1r}$ neurons on liraglutide-induced appetite suppression,[52] which suggests that alternative mechanisms might be engaged, at least acutely. Importantly, unlike most PVH neuronal populations, PVH^{AVP} neurons receive virtually no inputs from preproglucagon neurons and therefore might not be relevant to the signaling of brain-derived GLP-1.[53] Instead, GLP-1R in PVH^{AVP} neurons might be designed to specifically respond to peripheral GLP-1. How circulating GLP-1R agonists reach PVH^{AVP} neurons is unclear because these molecules do not cross the blood-brain-barrier and the PVH is distal from brain sites where their free diffusion occurs.[29,30] Here, we show that the GLP-1R is enriched in the axons of magnocellular neurons, at least at the level of the ME, creating a privileged site of access to peripherally injected GLP-1R agonists for these neurons. Consistently, we observed the accumulation of fluorescently labeled GLP-1R agonists in ME axons following a peripheral administration.

In summary, our findings identify a novel mechanism by which incretin therapies function to promote synergistic weight loss in the management of excess adiposity.

Limitations of study

The model used to delete *Gipr* from OLs only achieved partial deletion. Future work deleting *Gipr* from the entire OL lineage might uncover additional roles for GIPR signaling in OLs in energy and glucose homeostasis. In the model used in this study, although deletion of *Gipr* in OLs did not produce a marked change in metabolic phenotype, we did observe mild changes that might have altered the amplitude of the responses to incretin receptor agonists during the weight-loss intervention.

RESOURCE AVAILABILITY

Lead contact

Further information and requests for reagents may be directed to and will be fulfilled by the lead contact, Clemence Blouet (csb69@medschl.cam.ac.uk).

Materials availability

This study did not generate new unique reagents.

Data and code availability

- Data used to generate the figures are available in Data S1. Data have been deposited in the Zenodo repository (https://doi.org/10.5281/zenodo.15831198) and are publicly available. This paper analyzes existing, publicly available data, accessible on GEO (GEO: GSE133890). Microscopy data reported in this paper will be shared by the lead contact upon request.

- This paper does not report original code.
- Any additional information required to reanalyze the data reported in this paper is available from the lead contact upon request.

ACKNOWLEDGMENTS

We thank the Histopathology, Imaging, and Disease Model cores, in addition to the MRC MDU Mouse Biochemistry Laboratory, at the Wellcome-MRC Institute of Metabolic Science for their contributions. This work was supported by a Medical Research Council grant (MR/S011552/1; C.B.), a Wellcome Trust PhD Studentship (108926/Z/15/Z; R.H. and S.B.), Medical Research Council Metabolic Disease Unit and Mouse Biochemistry Laboratory grants (MC_UU_00014/5) and (MRC_MC_UU_12012/5), and a Wellcome Trust Strategic Award (208363/Z/17/Z). D.J.H. was supported by MRC (MR/S025618/1), Diabetes UK (22/0006389), and UKRI ERC Frontier research guarantee (EP/X026833/1) grants. This work was supported by the "Steve Morgan Foundation Type 1 Diabetes Grand Challenge" of Diabetes UK and SMF (grant number 23/0006627 to D.J.H. and J.B.). This project has received funding from the European Union's Horizon Europe Framework Programme (deuter O.N., grant agreement no. 101042046 to J.B.). For the purpose of open access, the author has applied a Creative Commons Attribution (CC BY) license to any author accepted manuscript version arising from this submission.

AUTHOR CONTRIBUTIONS

R.J.S., S.B., S.P., and C.B. designed the experiments; R.H., S.B., A.H.T., S.B., E.E., V.P., T.B., and A.A. executed experiments; R.H., S.B., A.A., V.P., and C.B. analyzed the data; R.H., C.B., and R.J.S. wrote the manuscript.

DECLARATION OF INTERESTS

R.J.S., S.P., and V.P. are employees and shareholders of Eli Lilly and Company. D.J.H. and J.B. have filed a patent on GLP-1R and GIPR chemical probes. D.J.H. and J.B. received licensing revenue from Celtarys Research for provision of GLP-1R/GIPR chemical probes. D.J.H. has filed patents related to type 2 diabetes therapy and GLP-1R agonism.

STAR★METHODS

Detailed methods are provided in the online version of this paper and include the following:

- KEY RESOURCES TABLE
- EXPERIMENTAL MODEL AND SUBJECT DETAILS
- METHOD DETAILS
  - Tamoxifen preparation and administration
  - GLP-1R and GIPR agonist preparation and administration
  - EdU chase experiment
  - Brain tissue preparation
  - Fluorescent in situ hybridization
  - Immunofluorescence
  - Light-sheet imaging
  - Super-resolution microscopy
  - Image analysis
  - Quantitative polymerase chain reaction
  - Metabolic phenotyping
  - Glycemic control phenotyping
  - Stereotaxic surgery, viral injections and chemogenetic studies
  - Oil Red O staining
- STATISTICAL ANALYSIS

SUPPLEMENTAL INFORMATION

Supplemental information can be found online at https://doi.org/10.1016/j.cmet.2025.07.009.

Received: July 8, 2024
Revised: April 7, 2025
Accepted: July 21, 2025
Published: August 13, 2025

REFERENCES

1. Drucker, D.J. (2013). Incretin action in the pancreas: potential promise, possible perils, and pathological pitfalls. Diabetes *62*, 3316–3323. https://doi.org/10.2337/db13-0822.
2. Hammoud, R., and Drucker, D.J. (2023). Beyond the pancreas: contrasting cardiometabolic actions of GIP and GLP1. Nat. Rev. Endocrinol. *19*, 201–216. https://doi.org/10.1038/s41574-022-00783-3.
3. Zhang, Q., Delessa, C.T., Augustin, R., Bakhti, M., Colldén, G., Drucker, D. J., Feuchtinger, A., Caceres, C.G., Grandl, G., Harger, A., et al. (2021). The glucose-dependent insulinotropic polypeptide (GIP) regulates body weight and food intake via CNS-GIPR signaling. Cell Metab. *33*, 833–844.e5. https://doi.org/10.1016/j.cmet.2021.01.015.
4. Heise, T., Mari, A., DeVries, J.H., Urva, S., Li, J., Pratt, E.J., Coskun, T., Thomas, M.K., Mather, K.J., Haupt, A., et al. (2022). Effects of subcutaneous tirzepatide versus placebo or semaglutide on pancreatic islet function and insulin sensitivity in adults with type 2 diabetes: a multicentre, randomised, double-blind, parallel-arm, phase 1 clinical trial. Lancet Diabetes Endocrinol. *10*, 418–429. https://doi.org/10.1016/S2213-8587(22)00085-7.
5. Frías, J.P., Davies, M.J., Rosenstock, J., Pérez Manghi, F.C., Fernández Landó, L., Bergman, B.K., Liu, B., Cui, X., and Brown, K.; SURPASS-2 Investigators (2021). Tirzepatide versus Semaglutide Once Weekly in Patients with Type 2 Diabetes. N. Engl. J. Med. *385*, 503–515. https://doi.org/10.1056/NEJMoa2107519.
6. Finan, B., Ma, T., Ottaway, N., Müller, T.D., Habegger, K.M., Heppner, K. M., Kirchner, H., Holland, J., Hembree, J., Raver, C., et al. (2013). Unimolecular dual incretins maximize metabolic benefits in rodents, monkeys, and humans. Sci. Transl. Med. *5*, 209ra151. https://doi.org/10.1126/scitranslmed.3007218.
7. Adriaenssens, A.E., Biggs, E.K., Darwish, T., Tadross, J., Sukthankar, T., Girish, M., Polex-Wolf, J., Lam, B.Y., Zvetkova, I., Pan, W., et al. (2019). Glucose-Dependent Insulinotropic Polypeptide Receptor-Expressing Cells in the Hypothalamus Regulate Food Intake. Cell Metab. *30*, 987–996.e6. https://doi.org/10.1016/j.cmet.2019.07.013.
8. Adriaenssens, A., Broichhagen, J., de Bray, A., Ast, J., Hasib, A., Jones, B., Tomas, A., Burgos, N.F., Woodward, O., Lewis, J., et al. (2023). Hypothalamic and brainstem glucose-dependent insulinotropic polypeptide receptor neurons employ distinct mechanisms to affect feeding. JCI Insight *8*, e164921. https://doi.org/10.1172/jci.insight.164921.
9. Steuernagel, L., Lam, B.Y.H., Klemm, P., Dowsett, G.K.C., Bauder, C.A., Tadross, J.A., Hitschfeld, T.S., del Rio Martin, A., Chen, W., de Solis, A. J., et al. (2022). HypoMap—a unified single-cell gene expression atlas of the murine hypothalamus. Nat. Metab. *4*, 1402–1419. https://doi.org/10.1038/s42255-022-00657-y.
10. Dowsett, G.K.C., Lam, B.Y.H., Tadross, J.A., Cimino, I., Rimmington, D., Coll, A.P., Polex-Wolf, J., Knudsen, L.B., Pyke, C., and Yeo, G.S.H. (2021). A survey of the mouse hindbrain in the fed and fasted states using single-nucleus RNA sequencing. Mol. Metab. *53*, 101240. https://doi.org/10.1016/j.molmet.2021.101240.
11. Kohnke, S., Buller, S., Nuzzaci, D., Ridley, K., Lam, B., Pivonkova, H., Bentsen, M.A., Alonge, K.M., Zhao, C., Tadross, J., et al. (2021). Nutritional regulation of oligodendrocyte differentiation regulates perineuronal net remodeling in the median eminence. Cell Rep. *36*, 109362. https://doi.org/10.1016/j.celrep.2021.109362.
12. Smith, C., Patterson-Cross, R., Woodward, O., Lewis, J., Chiarugi, D., Merkle, F., Gribble, F., Reimann, F., and Adriaenssens, A. (2022). A comparative transcriptomic analysis of glucagon-like peptide-1 receptor- and glucose-dependent insulinotropic polypeptide receptor-expressing cells in the hypothalamus. Appetite *174*, 106022. https://doi.org/10.1016/j.appet.2022.106022.

13. Tadross, J.A., Steuernagel, L., Dowsett, G.K.C., Kentistou, K.A., Lundh, S., Porniece-Kumar, M., Klemm, P., Rainbow, K., Hvid, H., Kania, K., et al. (2023). Human HYPOMAP: A comprehensive spatio-cellular map of the human hypothalamus. Preprint at bioRxiv, 2023.2009.2015.557967. https://doi.org/10.1101/2023.09.15.557967.

14. Borner, T., Reiner, B.C., Crist, R.C., Furst, C.D., Doebley, S.A., Halas, J.G., Ai, M., Samms, R.J., De Jonghe, B.C., and Hayes, M.R. (2023). GIP receptor agonism blocks chemotherapy-induced nausea and vomiting. Mol. Metab. *73*, 101743. https://doi.org/10.1016/j.molmet.2023.101743.

15. Borner, T., Geisler, C.E., Fortin, S.M., Cosgrove, R., Alsina-Fernandez, J., Dogra, M., Doebley, S., Sanchez-Navarro, M.J., Leon, R.M., Gaisinsky, J., et al. (2021). GIP Receptor Agonism Attenuates GLP-1 Receptor Agonist-Induced Nausea and Emesis in Preclinical Models. Diabetes *70*, 2545–2553. https://doi.org/10.2337/db21-0459.

16. Liskiewicz, A., Khalil, A., Liskiewicz, D., Novikoff, A., Grandl, G., Maity-Kumar, G., Gutgesell, R.M., Bakhti, M., Bastidas-Ponce, A., Czarnecki, O., et al. (2023). Glucose-dependent insulinotropic polypeptide regulates body weight and food intake via GABAergic neurons in mice. Nat. Metab. *5*, 2075–2085. https://doi.org/10.1038/s42255-023-00931-7.

17. Buller, S., Kohnke, S., Hansford, R., Shimizu, T., Richardson, W.D., and Blouet, C. (2023). Median eminence myelin continuously turns over in adult mice. Mol. Metab. *69*, 101690. https://doi.org/10.1016/j.molmet.2023.101690.

18. Marques, S., Zeisel, A., Codeluppi, S., van Bruggen, D., Mendanha Falcão, A., Xiao, L., Li, H., Häring, M., Hochgerner, H., Romanov, R.A., et al. (2016). Oligodendrocyte heterogeneity in the mouse juvenile and adult central nervous system. Science *352*, 1326–1329. https://doi.org/10.1126/science.aaf6463.

19. Zhang, Z.H., Ma, F.F., Zhang, H., and Xu, X.H. (2017). MARCKS is Necessary for Oligodendrocyte Precursor Cell Maturation. Neurochem. Res. *42*, 2933–2939. https://doi.org/10.1007/s11064-017-2324-7.

20. Yamane, S., Harada, N., and Inagaki, N. (2016). Mechanisms of fat-induced gastric inhibitory polypeptide/glucose-dependent insulinotropic polypeptide secretion from K cells. J. Diabetes Investig. *7*, 20–26. https://doi.org/10.1111/jdi.12467.

21. Ozarkar, S.S., Patel, R.K.R., Vulli, T., Friar, C.A., Burette, A.C., and Philpot, B.D. (2025). Regional analysis of myelin basic protein across postnatal brain development of C57BL/6J mice. Front. Neuroanat. *19*, 1535745. https://doi.org/10.3389/fnana.2025.1535745.

22. Fukushima, A. (2013). DiffCorr: an R package to analyze and visualize differential correlations in biological networks. Gene *518*, 209–214. https://doi.org/10.1016/j.gene.2012.11.028.

23. Tripathi, R.B., Jackiewicz, M., McKenzie, I.A., Kougioumtzidou, E., Grist, M., and Richardson, W.D. (2017). Remarkable Stability of Myelinating Oligodendrocytes in Mice. Cell Rep. *21*, 316–323. https://doi.org/10.1016/j.celrep.2017.09.050.

24. McKenzie, I.A., Ohayon, D., Li, H., de Faria, J.P., Emery, B., Tohyama, K., and Richardson, W.D. (2014). Motor skill learning requires active central myelination. Science *346*, 318–322. https://doi.org/10.1126/science.1254960.

25. Fard, M.K., van der Meer, F., Sánchez, P., Cantuti-Castelvetri, L., Mandad, S., Jäkel, S., Fornasiero, E.F., Schmitt, S., Ehrlich, M., Starost, L., et al. (2017). BCAS1 expression defines a population of early myelinating OLs in multiple sclerosis lesions. Sci. Transl. Med. *9*, eaam7816. https://doi.org/10.1126/scitranslmed.aam7816.

26. Lettieri, A., Oleari, R., van den Munkhof, M.H., van Battum, E.Y., Verhagen, M.G., Tacconi, C., Spreafico, M., Paganoni, A.J.J., Azzarelli, R.,, Andre', V., et al. (2023). SEMA6A drives GnRH neuron-dependent puberty onset by tuning median eminence vascular permeability. Nat. Commun. *14*, 8097. https://doi.org/10.1038/s41467-023-43820-z.

27. Buller, S., Staricoff, E.O., Riches, C., Tsang, A., Josipovic, M., Ikemura, K., Opoku, G., Sato, I., Hirohata, S., Stenzel, S., et al. (2024). Adult oligodendrogenesis gates arcuate neuronal glucose sensing through remodelling of the blood-hypothalamus barrier via ADAMTS4. Preprint at bioRxiv, 2024.2009.2010.612227. https://doi.org/10.1101/2024.09.10.612227.

28. Salameh, T.S., Rhea, E.M., Talbot, K., and Banks, W.A. (2020). Brain uptake pharmacokinetics of incretin receptor agonists showing promise as Alzheimer's and Parkinson's disease therapeutics. Biochem. Pharmacol. *180*, 114187. https://doi.org/10.1016/j.bcp.2020.114187.

29. Gabery, S., Salinas, C.G., Paulsen, S.J., Ahnfelt-Rønne, J., Alanentalo, T., Baquero, A.F., Buckley, S.T., Farkas, E., Fekete, C., Frederiksen, K.S., et al. (2020). Semaglutide lowers body weight in rodents via distributed neural pathways. JCI Insight *5*, e133429. https://doi.org/10.1172/jci.insight.133429.

30. Skovbjerg, G., Roostalu, U., Salinas, C.G., Skytte, J.L., Perens, J., Clemmensen, C., Elster, L., Frich, C.K., Hansen, H.H., and Hecksher-Sørensen, J. (2023). Uncovering CNS access of lipidated exendin-4 analogues by quantitative whole-brain 3D light sheet imaging. Neuropharmacology *238*, 109637. https://doi.org/10.1016/j.neuropharm.2023.109637.

31. Pastor, F.E., Blázquez, J.L., Toranzo, D., Peláez, B., Sánchez, A., Alvarez-Morujo, A.J., and Amat, P. (1991). Myelinated Herring bodies in the median eminence of the cat. Histol. Histopathol. *6*, 161–165.

32. Nagai, Y., Miyakawa, N., Takuwa, H., Hori, Y., Oyama, K., Ji, B., Takahashi, M., Huang, X.P., Slocum, S.T., DiBerto, J.F., et al. (2020). Deschloroclozapine, a potent and selective chemogenetic actuator enables rapid neuronal and behavioral modulations in mice and monkeys. Nat. Neurosci. *23*, 1157–1167. https://doi.org/10.1038/s41593-020-0661-3.

33. Woodruff, R.H., Fruttiger, M., Richardson, W.D., and Franklin, R.J.M. (2004). Platelet-derived growth factor regulates oligodendrocyte progenitor numbers in adult CNS and their response following CNS demyelination. Mol. Cell. Neurosci. *25*, 252–262. https://doi.org/10.1016/j.mcn.2003.10.014.

34. Mei, F., Christin Chong, S.Y., and Chan, J.R. (2013). Myelin-based inhibitors of oligodendrocyte myelination: clues from axonal growth and regeneration. Neurosci. Bull. *29*, 177–188. https://doi.org/10.1007/s12264-013-1319-x.

35. Baer, A.S., Syed, Y.A., Kang, S.U., Mitteregger, D., Vig, R., Ffrench-Constant, C., Franklin, R.J.M., Altmann, F., Lubec, G., and Kotter, M.R. (2009). Myelin-mediated inhibition of oligodendrocyte precursor differentiation can be overcome by pharmacological modulation of Fyn-RhoA and protein kinase C signalling. Brain *132*, 465–481. https://doi.org/10.1093/brain/awn334.

36. Campbell, J.E., Ussher, J.R., Mulvihill, E.E., Kolic, J., Baggio, L.L., Cao, X., Liu, Y., Lamont, B.J., Morii, T., Streutker, C.J., et al. (2016). TCF1 links GIPR signaling to the control of beta cell function and survival. Nat. Med. *22*, 84–90. https://doi.org/10.1038/nm.3997.

37. Zhao, C., Deng, Y., Liu, L., Yu, K., Zhang, L., Wang, H., He, X., Wang, J., Lu, C., Wu, L.N., et al. (2016). Dual regulatory switch through interactions of Tcf7l2/Tcf4 with stage-specific partners propels oligodendroglial maturation. Nat. Commun. *7*, 10883. https://doi.org/10.1038/ncomms10883.

38. Thaler, J.P., Yi, C.X., Schur, E.A., Guyenet, S.J., Hwang, B.H., Dietrich, M.O., Zhao, X., Sarruf, D.A., Izgur, V., Maravilla, K.R., et al. (2012). Obesity is associated with hypothalamic injury in rodents and humans. J. Clin. Invest. *122*, 153–162. https://doi.org/10.1172/JCI59660.

39. Samms, R.J., Christe, M.E., Collins, K.A., Pirro, V., Droz, B.A., Holland, A.K., Friedrich, J.L., Wojnicki, S., Konkol, D.L., Cosgrove, R., et al. (2021). GIPR agonism mediates weight-independent insulin sensitization by tirzepatide in obese mice. J. Clin. Invest. *131*, e146353. https://doi.org/10.1172/JCI146353.

40. Yoneshiro, T., Wang, Q., Tajima, K., Matsushita, M., Maki, H., Igarashi, K., Dai, Z., White, P.J., McGarrah, R.W., Ilkayeva, O.R., et al. (2019). BCAA catabolism in brown fat controls energy homeostasis through SLC25A44. Nature *572*, 614–619. https://doi.org/10.1038/s41586-019-1503-x.

41. Samms, R.J., Zhang, G., He, W., Ilkayeva, O., Droz, B.A., Bauer, S.M., Stutsman, C., Pirro, V., Collins, K.A., Furber, E.C., et al. (2022). Tirzepatide induces a thermogenic-like amino acid signature in brown

adipose tissue. Mol. Metab. *64*, 101550. https://doi.org/10.1016/j.molmet.2022.101550.

42. Zhang, C., Vincelette, L.K., Reimann, F., and Liberles, S.D. (2022). A brainstem circuit for nausea suppression. Cell Rep. *39*, 110953. https://doi.org/10.1016/j.celrep.2022.110953.
43. Esser, S., Lampugnani, M.G., Corada, M., Dejana, E., Risau, W., Zhang, Z. G., Zhang, L., Jiang, Q., Zhang, R., and Davies, K. (1998). Vascular endothelial growth factor induces VE-cadherin tyrosine phosphorylation in endothelial cells VEGF. J. Cell Sci. *111*, 1853–1865. https://doi.org/10.1242/jcs.111.13.1853.
44. Zhang, Z.G., Zhang, L., Jiang, Q., Zhang, R., Davies, K., Powers, C., Bruggen, N., and Chopp, M. (2000). VEGF enhances angiogenesis and promotes blood-brain barrier leakage in the ischemic brain. J. Clin. Invest. *106*, 829–838. https://doi.org/10.1172/JCI9369.
45. Romanò, N., Lafont, C., Campos, P., Guillou, A., Fiordelisio, T., Hodson, D. J., Mollard, P., and Schaeffer, M. (2023). Median eminence blood flow influences food intake by regulating ghrelin access to the metabolic brain. JCI Insight *8*, e165763. https://doi.org/10.1172/jci.insight.165763.
46. Langlet, F., Levin, B.E., Luquet, S., Mazzone, M., Messina, A., Dunn-Meynell, A. A., Balland, E., Lacombe, A., Mazur, D., Carmeliet, P., et al. (2013). Tanycytic VEGF-A Boosts Blood-Hypothalamus Barrier Plasticity and Access of Metabolic Signals to the Arcuate Nucleus in Response to Fasting. Cell Metab. *17*, 607–617. https://doi.org/10.1016/j.cmet.2013.03.004.
47. Langhans, W., Delprete, E., and Scharrer, E. (1991). Mechanisms of vasopressin's anorectic effect. Physiol. Behav. *49*, 169–176. https://doi.org/10.1016/0031-9384(91)90251-l.
48. Yoshimura, M., Nishimura, K., Nishimura, H., Sonoda, S., Ueno, H., Motojima, Y., Saito, R., Maruyama, T., Nonaka, Y., and Ueta, Y. (2017). Activation of endogenous arginine vasopressin neurons inhibit food intake: by using a novel transgenic rat line with DREADDs system. Sci. Rep. *7*, 15728. https://doi.org/10.1038/s41598-017-16049-2.
49. Pei, H., Sutton, A.K., Burnett, K.H., Fuller, P.M., and Olson, D.P. (2014). AVP neurons in the paraventricular nucleus of the hypothalamus regulate feeding. Mol. Metab. *3*, 209–215. https://doi.org/10.1016/j.molmet.2013.12.006.
50. Mohan, S., Flatt, P.R., Irwin, N., and Moffett, R.C. (2021). Weight-reducing, lipid-lowering and antidiabetic activities of a novel arginine vasopressin analogue acting at the V1a and V1b receptors in high-fat-fed mice. Diabetes Obes. Metab. *23*, 2215–2225. https://doi.org/10.1111/dom.14462.
51. McMahon, L.R., and Wellman, P.J. (1998). PVN infusion of GLP-1-(7–36) amide suppresses feeding but does not induce aversion or alter locomotion in rats. Am. J. Physiol. *274*, R23–R29. https://doi.org/10.1152/ajpregu.1998.274.1.R23.
52. Li, M.M., Madara, J.C., Steger, J.S., Krashes, M.J., Balthasar, N., Campbell, J.N., Resch, J.M., Conley, N.J., Garfield, A.S., and Lowell, B. B. (2019). The Paraventricular Hypothalamus Regulates Satiety and Prevents Obesity via Two Genetically Distinct Circuits. Neuron *102*, 653–667.e6. https://doi.org/10.1016/j.neuron.2019.02.028.
53. Tauchi, M., Zhang, R., D'Alessio, D.A., Stern, J.E., and Herman, J.P. (2008). Distribution of glucagon-like peptide-1 immunoreactivity in the hypothalamic paraventricular and supraoptic nuclei. J. Chem. Neuroanat. *36*, 144–149. https://doi.org/10.1016/j.jchemneu.2008.07.009.
54. Coskun, T., Urva, S., Roell, W.C., Qu, H., Loghin, C., Moyers, J.S., O'Farrell, L.S., Briere, D.A., Sloop, K.W., Thomas, M.K., et al. (2022). LY3437943, a novel triple glucagon, GIP, and GLP-1 receptor agonist for glycemic control and weight loss: From discovery to clinical proof of concept. Cell Metab. *34*, 1234–1247.e9. https://doi.org/10.1016/j.cmet.2022.07.013.

STAR★METHODS

KEY RESOURCES TABLE

REAGENT OR RESOURCE	SOURCE	IDENTIFIER
Antibodies		
Alexa-Fluor® 488 AffiniPure donkey anti-chicken, 1:500 dilution	Jackson Immunoresearch	Cat# 703-545-155; RRID: AB_2340375
Donkey anti-goat Alexa Fluor® 488-conjugate, 1:500 dilution	Life Technologies	Cat# A11055; RRID: AB_2534102
Donkey anti-goat Alexa Fluor® 647-conjugate, 1:500 dilution	Life Technologies	Cat# A21447; RRID: AB_2535864
Donkey anti-mouse Alexa Fluor® 594-conjugate, 1:500 dilution	Life Technologies	Cat# A21203; RRID: AB_141633
Donkey anti-rabbit Alexa Fluor® 488-conjugate, 1:500 dilution	Life Technologies	Cat# A21206; RRID: AB_2535792
Donkey anti-rabbit Alexa Fluor® 555-conjugate, 1:500 dilution	Life Technologies	Cat# A31572; RRID: AB_162543
Donkey anti-rabbit Alexa Fluor® 594-conjugate, 1:500 dilution	Life Technologies	Cat# A21207; RRID: AB_141637
Donkey anti-rat Alexa Fluor® 488-conjugate, 1:500 dilution	Life Technologies	Cat# A21208; RRID: AB_141709
Donkey anti-rat Alexa Fluor® 594-conjugate, 1:500 dilution	Life Technologies	Cat# A21209; RRID: AB_2535795
Donkey anti-rat Alexa Fluor® 647-conjugate, 1:500 dilution	Life Technologies	Cat# A78947; RRID: AB_2910635
Chicken anti-GFP, 1:1000 dilution	Abcam	Cat# ab13970; RRID: AB_300798
Goat anti-Sox10, 1:50 dilution	R&D Systems	Cat# AF2864; RRID: AB_442208
Rabbit anti-PDGFRa, 1:500 dilution	Cell Signaling Technologies	Cat# 3164; RRID: AB_2162351
Rat anti-MBP, 1:500 dilution	Abcam	Cat# ab7349; RRID: AB_305869
GLP-1R, 1:500 dilution	Abcam	ab218532; RRID: AB_2864762
AVP, 1:2000 dilution	Abcam	ab213708; RRID: AB_2062095
Chemicals, peptides, and recombinant proteins		
Tamoxifen, prepared at 20–30 mg/ml in corn oil	Sigma	Cat# T5648
Corn oil	Sigma	Cat# C82276
LAGIPRA, GIP-085	Eli Lilly and Company	N/A
LAGLP-1RA, semaglutide	Eli Lilly and Company	N/A
SAGLP-1RAIR800	Eli Lilly and Company	N/A
GIPRACy5	Goft from Johannes Broichhagen	N/A
RNEasy Micro Kit	Qiagen	Cat# 74004
RNAlater Solution	ThermoFisher	Cat# AM7021
High Capacity cDNA Reverse Transcription Kit	Applied Biosystems	Cat# 4368814
2X SYBR Green PCR Master Mix	Applied Biosystems	Cat# 4344463
2X Taqman Universal PCR Master Mix	Applied Biosystems	Cat# 4305719
C57BL/6J	Charles Rivers	N/A
Mouse(Plp1-cre/ERT)3Pop	Jackson Laboratories	MGI 2450391
Opalin-CreERT2; Tg(Opalin-icre/ERT2)#Rjfl	Richardson Lab, University College London	MGI 5763107
R26R-eYFP: Gt(ROSA)26Sortm1 (EYFP)Cos	Jackson Laboratories	MGI 2449038
Ai9: Gt(ROSA)26Sortm9(CAG-tdTomato)Hze	Jackson Laboratories	MGI 3809523

(*Continued on next page*)

Continued		
REAGENT OR RESOURCE	SOURCE	IDENTIFIER
Software and algorithms		
Prism 9.0	GraphPad	https://www.graphpad.com/scientific-software/prism/
ImageJ (Fiji)	ImageJ	https://imagej.nih.gov/ij/index.html
Imaris		
R	R	https://www.r-project.org/
Critical commercial assays		
Mm-*Gipr*-C1 D54	ACD	Cat# 319121
Mm-Sox10-C4		Cat# 435931
Mm-Pdgfra-C3		Cat# 480661
Mm-Plp1-C2		Cat# 428181
Mm-Sox10-C2		Cat# 435938
Mm-Bmp4-C1		Cat# 401308
Oligonucleotides		
Gipr	TGCAGGCTTTGTCTTCCGCCAGTG	N/A
	GCGTCTGGTCCTGAAAAGCCCCATT	N/A
Gapdg	AGGTCGGTGTGAACGGATTTG	N/A
	TGTAGACCATGTAGTTGAGGTCA	N/A
Other		
Rodent chow	SAFE	Cat# SAFE R105
60% high fat diet (HFD)	Research Diets	Cat# D12451i

Details of all reagents and animal models are detailed in the key resources table.

EXPERIMENTAL MODEL AND SUBJECT DETAILS

All animal experiments were performed in accordance with the UK Home Office regulations under the Animals (Scientific Procedures) Act (1986) and with the approval of the University of Cambridge Animal Welfare and Ethics Review Board. Animals were group-housed in a specific pathogen free facility and maintained on a standard 12-hour light/dark cycle (lights on 7:00–19:00) at 22 °C with *ad libitum* access to water and standard laboratory chow unless otherwise stated. All experiments were performed on male mice starting from postnatal day 60 (P60). All dietary and pharmacological treatments were assigned randomly in body-weight matched groups. Mice were acclimatised to the dosing procedures for at least 4 consecutive days before chronic dosing studies.

METHOD DETAILS

Tamoxifen preparation and administration

Tamoxifen was prepared in corn oil by sonication at 37 °C at 30 mg/ml prior to administration by oral gavage at 300 mg/kg on 4 consecutive days in *Opalin-Cre/ERT2;Ai9* mice, or through the intraperitoneal at 80 mg/kg for 8 consecutive days in *Plp-Cre/ERT2* mice.

GLP-1R and GIPR agonist preparation and administration

The LAGIPRA, LAGLP-1RA and SAGLP-1RA^{IR800} were synthesized at Eli Lilly and Company, dissolved in 40mM Tris-HCl pH8 with 0.02% PS-80, and dose subcutaneously or intravenously at 300nmol/kg, 100nmol/kg and 100nmol/kg, respectively. LAGIPRA, LAGLP-1RA were dosed at ZT8-ZT9. Before SAGLP-1RA^{IR800} administration, mice were fasted for 4h. The GIPRA^{cy5} was prepared a previously described[8] and dosed intravenously at 100nmol/kg.

EdU chase experiment

Mice were administered EdU through 4 intraperitoneal injections (50 mg/kg; prepared in sterile saline at 5 mg/ml; 1 injection every 6h) during the 24h preceding terminal perfusion.

Brain tissue preparation

Animals were anaesthetized with an ip injection of 50 ul pentobarbitol (Dolethal, 200 mg/ml) then transcardially perfused as follows. For immunohistochemistry (IHC), animals were perfused with 0.01 M phosphate buffered saline (PBS) at room temperature (RT)

followed by 4% paraformaldehyde in PBS (pH 7.4) at 4°C. For clearing experiments, animals were perfused with 0.01 M phosphate buffered saline (PBS) at room temperature (RT) followed 10% NBF. For RNA-scope experiments, the brain is collected and quick frozen on crushed dry ice and stored at -80°C until further use.

Fluorescent in situ hybridization

Multiplexed fluorescent in situ hybridizations (ISH) in brain slices were conducted using RNAscope technology (Advanced Cell Diagnostics, Newark, CA). Each brain was divided into forebrain and hindbrain by a coronal cut at the level of the pons and mounted on the precooled cryostat holder with Tissue-Tek O.C.T. compound (Sakura Finetek). 12 μm thick coronal sections covering the 1) ME/ARH 2) VTA/SN 3) AP/NTS and 4) spinal cord/dorsal horn were collected on SuperFrost Plus microscope slides. ISH was performed on tissue sections using the RNAscopeTM Multiplex Fluorescent V2 Assay (Advanced Cell Diagnostics, Cat. 323100) to simultaneously visualize up to four different mRNAs using target specific probes. Appropriate negative and positive controls were included and run in parallel. RNAscope assay was performed according to the manufacturer's user manual. After ISH, sections were counterstained with DAPI and coverslipped using a fluorescence mounting medium. Finally, slides were scanned under a 20X objective in an Olympus VS-120 slide scanner with appropriate fluorescent filters. Densities of cells per mm2 were obtained for 3 sections per animal.

Immunofluorescence

Brains were post-fixed overnight at 4 °C in 4% PFA then cryoprotected in 30% (w/v) sucrose (Fisher Scientific) solution in PBS for at least 48 h prior to processing. Tissues were covered with Optimal Cutting Temperature (OCT) medium (CellPath, Newtown, UK) and sections were obtained at 25 μm on a Leica SM2010R Freezing Microtome (Leica, Wetzlar, Germany). All sections were subjected to heat-mediated antigen retrieval in 10 mM sodium citrate (pH6.5; Fisher Scientific) in distilled water for 20 min at 80 °C prior to washing 3 times in PBS. For all experiments, sections were blocked in normal donkey serum (NDS, Vector Biolabs, Philadelphia, Pennsylvania) diluted in PBS containing 0.3% Triton X-100 (0.3% PBST; Sigma) for 1 h prior to primary antibody incubation overnight at 4 °C. Following primary antibody incubation, sections were washed 3 time with 0.1% PBST and incubated with appropriate fluorophore-conjugated secondary antibodies diluted 1:500 in 0.3% PBST for 2 h at room temperature. Sections were subsequently washed with 0.1% PBST and mounted to Clarity microscope slides (Dixon Science, Edenbridge, UK) under coverslips (1.0 thickness; Marienfeld, Lauda-Königshofen, Germany) with Vectashield Vibrance Mounting Medium with 4′,6-diamidino-2-phenylindole (DAPI; Vector Laboratories, Newark, California). Alexa405, Alexa488, Alexa555, Alexa594 and Alexa647 conjugates (Life Technologies, Carlsbad, California) were used as secondary antibodies.

Tissue Clearing Brains were dissected and immersion fixed in NBF overnight at room temperature. The samples were then washed 3×30 minutes in PBS with shaking. Tissue was dehydrated in MeOH/H2O series: 20%, 40%, 60%, 80% and 100%, for 1 hour each, at room temperature. Samples were incubated in 100% MeOH overnight and the next day for 3 hours (with shaking) in 66% DCM/33% MeOH at room temperature and in 100% DCM for 15 minutes twice (with shaking) to remove traces of methanol. The samples were finally transferred to Dibenzyl Ether (DBE) and stored in closed glass vials in the dark.

Light-sheet imaging

All samples were imaged using a Lavision ultramicroscope system II and MV PLAPO 2X C objective. Whole mouse brains were imaged at 1.26 × magnification. In addition, the medio basal hypothalamus was imaged at 4 x magnification. The fluorescent signal was captured at the autofluorescence channel (560nm) and compound-specific channel (790nm). DBE is used as a clearing agent during the acquisition of data. The Imaris software was used to visualize the data in 3D.

Confocal microscopy: For all experiments, slides and images were blinded to experimental condition. Sections were imaged with a Leica SP8 confocal microscope using either a 40× or 63× oil objective. Sections were imaged as z-stacks at intervals of 0.3 μm with tile scanning to obtain signal from the entire depth and area of the region of interest (ROI). Microscope settings were identical for image acquisition within each experiment. Images were analysed using Fiji software.

Super-resolution microscopy

Following standard immunohistochemistry procedure described above and the wash step of the secondary antibody, samples were incubated in Hoechst 33342 (1:10,000 in PBS, Invitrogen) for 5 minutes, then washed three times for 5 minutes each in PBS. Sections were subsequently mounted onto Clarity microscope slides (Dixon Science) using 1.5H coverslips (Carl Zeiss) and ProLong Diamond Mounting Medium (Thermo Fisher). The slides were left to dry at room temperature overnight before being stored long-term at 4°C. Imaging was performed using an LSM 980 confocal microscope (Zeiss) equipped with Airyscan. Appropriate long-pass (LP) and band-pass (BP) filters were applied during acquisition to minimize channel bleed-through. Initial Airyscan post-processing was conducted using Zen Black software (Zeiss), with further image processing and export performed in Fiji (ImageJ). All imaging conditions were maintained identically between slides.

Image analysis

Images obtained from cleared brains using light sheet microscopy were analysed as previously described.[30] Images obtained from RNAscope experiments were imported into the VIS software (Visiopharm, Denmark) for ah-hoc analysis. Images acquired using confocal microscopy were processed as follows. Three or more sections per animal were used for quantification. All confocal images

were analysed using Fiji software. Prior to analysis, z-stacks were projected into a single image and the image scale calibrated to determine cell density (number of cells/unit area). The area of ROIs were calculated by tracing the ROI with the freehand tool and measuring - all ROI borders were determined using the Paxinos and Franklin Mouse Brain Atlas. Cells labelled for specific markers, alone or in combination with others, were counted using the Manual Cell Counter Fiji Plugin. The identity of each biological sample was revealed once all analysis for a given experiment was complete.

Quantitative polymerase chain reaction

Fresh hypothalami were collected into RNAlater solution (ThermoFisher) and stored at −20 °C until processing. RNA was extracted from tissues samples using an RNEasy Micro Kit following the manufacturer's protocol. 100–200 ng of total RNA was reverse transcribed to cDNA using the High Capacity cDNA Reverse Transcription Kit) according to the manufacturer's instructions. Gene expression was assessed using either SYBR Green or TaqMan technologies on a QuantStudio 5 (Applied Biosystems). Relative gene expression was calculated by the 2(-ΔΔCt) method. Data were normalised to the housekeeping gene *Gapdh*, as the expression of this gene did not change between groups. All primers and probes were obtained from Sigma–Aldrich and commercially available TaqMan assays were obtained from Thermo Fisher.

Metabolic phenotyping

Body composition was analysed using a EchoMRI Whole Body Composition Analyser (EchoMRI, Houston, Texas). Promethion High-Definition Multiplexed Respirometry Cages (Sable Systems International, Las Vegas, Nevada) were used to analyse energy expenditure by indirect calorimetry, food intake, water intake, respiratory quotient and activity over 48 h in mice single-house for at least one week prior. Data collected during the first 24 h of each run was discarded to allow for acclimatisation of mice to the altered cage environment.

Glycemic control phenotyping

For the oral glucose tolerance test, mice were food deprived for 6 hr and blood was sampled from tail vein immediately prior to glucose bolus (gavage, 2 mg/kg), and 10, 20, 30, 60, 90, and 120 min following bolus administration. For the insulin sensitivity test, mice were food deprived for 6 hr and blood was sampled from tail vein immediately prior to the administration of an insulin bolus (ip, 0.75U/kg), and 10, 20, 30, 60, 90, and 120 min following bolus administration. Blood glucose was analysed using an AlphaTrak3 handheld glucometer (Precision Xtra; MediSense).

Stereotaxic surgery, viral injections and chemogenetic studies

Surgical procedures were conducted on 9- to 11-week-old male AVP-Cre and wild-type littermate mice. All animals received Metacam prior to surgery and 24 h after surgery. Under isoflurane-induced anesthesia, 300nL AAV8-hSyn-DIO-hMD4(Gi)-mCherry (Titer 5 x 1012 genomic copies; University of North Carolina Viral Core facility, USA) were injected into the PVH (A/P: -0.70 mm, D/V: -4.75 mm, and lateral: +/− 0.25 mm from the bregma) with a bilateral steel guide cannula and a 33-gauge stainless steel injector (Plastics One). Following the surgery, mice were allowed for a 3 week recovery. After that, 5mg/ml deschloroclozapine (DCZ) or the same volume of vehicle DMSO were introduced to the drinking water and refreshed twice a week throughout the rest of study. Two weeks after the DCZ or DMSO introduction, the mice were single-housed for 1 week, following by daily subcutaneous injections of saline (50mL/kg) during ZT 8-10 for 1 week to obtain an individual baseline response to the procedures and then daily subcutaneous injections of liraglutide (0.2mg/kg; Tocris, UK) during the same time-of-day for another week. Food and animals were weighed daily during these 2 weeks. After the last treatment, mice were allowed to recover for 1 week while being maintained on DCZ- or DMSO- added drinking water. Mice were perfused with 4% PFA transcardially after the terminal treatments as indicated.

Oil Red O staining

PFA-fixed tissues were cryoprotected in 30% sucrose solution (w/v in distilled water; Sigma) overnight before sectioning at 8-10μm on a Leica CM1950 cryostat onto electrostatically charged slides. A stock solution of ORO was made up by gently heating 0.5 g ORO (Sigma) in 100 ml absolute isopropyl alcohol (Sigma) in a water bath overnight. A working solution was prepared by mixing 60 ml ORO stock solution and 40 ml 1% dextrin (Fisher Scientific) in distilled water. The working solution was allowed to stand for one day and then filtered. Slides were rinsed in PBS prior to incubation with ORO working solution for 20 minutes. Excess stain was rinsed off with distilled water and sections counterstained with haematoxylin for 20 seconds and blued in tap water. Coverslips were mounted with Pertex mounting medium (Pioneer Research Chemicals Ltd.). Images were acquired with an Axioscan Z1 Slide Scanner (Zeiss) using a 20x objective and analysed using the vacuoles module on HALO Image Analysis Software.

Targeted metabolomics

Targeted metabolomics was performed on plasma, liver, interscapular brown adipose tissue (iBAT), epididymal white adipose tissue (eWAT) and muscle samples using a liquid chromatography with tandem mass spectrometry (LC-MS/MS) approach, as described in [54]. Briefly, plasma samples were frozen immediately after collection and then thawed in an ice bath prior to LC-MS/MS analysis. Two extraction protocols (methods A and B) were used to collect metabolomics data. For method (A), 150 μL of pre-chilled acetonitrile-methanol (1:1 v/v) solvent mixture was added to 25-μL plasma aliquot. For method (B), 150 μL of pre-chilled methanol-water (4:1 v/v) solvent mixture was added to a second 25-μL plasma aliquot. Samples were mixed thoroughly and incubated at −20°C overnight. Both extraction solutions were spiked with a mix of stable labelled internal standards. After overnight extraction, the samples

were centrifuged for 15 minutes at 14000 g at +4°C. A pooled calibrator sample was created for each method by combining an aliquot of supernatant from all the extracted samples together. The pooled calibrator was serially diluted in the same extraction solvent and used to create a calibration curve (100% [pooled calibrator], 75%, 50%, 30%, 15%, 10%, and 5%) for relative quantitation and batch-to-batch data normalization. Individual samples were further diluted at 1:1 (v/v) ratio with each extraction solution, transferred into a new 96-well plate, and injected for LC-MS/MS analysis.

Tissue samples were flash frozen in liquid nitrogen immediately after collection and stored at −80 °C. Frozen tissue samples were pulverized using a tissue pulverizer and kept frozen until LC-MS/MS analysis. Two aliquots of pulverized tissue were weighted for each sample to run methods A and B independently. Tissue samples were extracted and processed as described above. Extraction solutions were added to reach a final concentration of 100 mg/mL.

Data were acquired using a Shimadzu Nexera X2 UPLC system coupled to an AB Sciex 6500+ triple quadrupole mass spectrometer equipped with an electrospray source. For method A, a Waters Acquity BEH amide 100 mm x 2.1 mm, 1.7 mm particle size, column was used; for method B, a Waters XSelect HSS T3 C18 100 mm x 2.1 mm, 1.8 mm particle size, column was used. Both columns were maintained at +40C. Elution solvents for both methods were 10 mM ammonium formate adjusted with 0.1% formic acid (solvent A) and 0.1% formic acid in acetonitrile (solvent B). Data were acquired using scheduled multiple reaction monitoring mode with polarity switching. A total of 250 polar metabolites were targeted. For most of the metabolites, identification was supported by 1 qualifier ion monitored in addition to a quantifier ion. Two qualifier ions were monitored to resolve interferences amongst few metabolites (data not shown). Peak areas were integrated using the AB SCIEX MultiQuant 3.0.2 software. Only analytes detected at the lowest pooled quality control calibrator with signal-to-noise >3 and detected in more than 75% of the individual samples were quantified. Relative quantitation to the pooled calibrators was achieved using a linear regression model. Metabolite areas were normalized to internal standard area responses. For analytes with no matching stable labelled internal standards, the optimal choice (picked amongst the internal standards monitored under the same polarity and within the same assay) was the internal standard giving the minimum root mean square error for the pooled calibrators and best linear fit. Individual sample values falling below the limit of detection were imputed to 1/2 times the lower calibrator.

For statistical analysis, the metabolomics data were log-transformed. On-way ANOVA with Dunnett's post hoc test was performed to assess significance ($p < 0.05$) of between-group data distributions for individual metabolites. Multivariate analysis of variance (MANOVA) was also performed on principal components arising from principal component analysis (PCA) to assess changes in metabolomic profile comprehensively. Spearman's rank correlations were calculated to explore the association between metabolites. DiffCorr package was used to identify pattern changes in correlation networks.[22] Statistical analyses were implemented by using Matlab R2019a (Mathworks) and R 3.6.0.

STATISTICAL ANALYSIS

All data visualisation and statistical analysis was performed in Prism 9 Software (GraphPad). or all statistical tests, an α risk of 5% was used. All kinetics were analysed using repeated-measures two-way ANOVAs and adjusted with post hoc tests. Multiple comparisons were tested with one-way ANOVAs and adjusted with Tukey's post hoc tests. Single comparisons were made using two-tail Student's t tests.